

Bachelor's Thesis

Charakterisierung von Pixel Sensoren für das ATLAS ITk Upgrade

Characterisation of Pixel Sensors for the ATLAS ITk Upgrade

prepared by

Johannes Weller

from Wildeshausen

at the II. Physikalischen Institut

Thesis number: II.Physik-UniGö-BSc-2020/04
Thesis period: 30th March 2020 until 17th July 2020
First referee: Prof. Dr. Arnulf Quadt
Second referee: Priv.Do. Dr. Jörn Große-Knetter

Zusammenfassung

In dieser Bachelorarbeit wird die Analyse von Leckstrom- und Kapazitätsmessungen an planaren Siliziumpixelsensoren präsentiert. Dafür wurde die Analysesoftware ROOT verwendet. Die Sensoren wurden für den neuen Vollsiliziumspurdetektor (ITk) des ATLAS-Teilchendetektors, welcher ein Experiment am „Large Hadron Collider“-Beschleuniger am CERN ist, entwickelt. Die analysierten Messungen wurden im Zuge der laufenden Marktstudie gemacht, um geeignete Produzenten für die kommende Produktionsphase zu finden. Im Folgenden wird gezeigt, wie ein Algorithmus zur Bestimmung der Verarmungsspannung aus den Kapazitäts-Spannungs-Charakteristiken von unbestrahlten Sensoren entwickelt wurde. Ein weiterer Algorithmus, der einen Leckstrom-Durchbruch aus den Strom-Spannungs-Charakteristiken eines unbestrahlten Sensors erkennen kann und die Durchbruchspannung mithilfe verschiedener Definitionen bestimmt, wurde entwickelt und an Sensoren mit verschiedenen Oberflächen und Dicken getestet.

Außerdem wurde die Temperaturabhängigkeit des Leckstroms in bestrahlten Sensoren analysiert, wobei ein enger Zusammenhang zwischen der gemessenen und der theoretisch vorhergesagten Abhängigkeit gefunden wurde. Die theoretische Abhängigkeit wurde benutzt, um den Leckstrom von der Messtemperatur auf eine andere Temperatur zu skalieren. Zuletzt wurde noch der absolute Leckstrom in Sensoren, die zu verschiedenen Fluenzen bestrahlt wurden und verschiedene Ausheilungszeiten erfahren haben, mit der theoretischen Erwartung verglichen, wobei sich zeigte, dass das Verhalten des gemessenen Leckstroms grob mit der theoretischen Vorhersage eines zur Fluenz proportionalen Leckstroms übereinstimmt.

Abstract

In this bachelor thesis, the analysis of leakage current and capacitance measurements of planar Silicon pixel sensors is presented. For this analysis the software ROOT was used. The sensors were developed for the new full Silicon Inner Tracker (ITk) of the ATLAS particle detector, which is an experiment at the Large Hadron Collider at CERN. The measurements that were analysed were made in the course of the ongoing market survey in order to find suitable foundries for the upcoming production phase.

In the following, it is shown how an algorithm to determine the depletion voltage from capacitance-voltage-characteristics of unirradiated sensors was developed and tested. Another algorithm to detect the current breakdown of an unirradiated sensor from the current-voltage-curves and to determine the breakdown voltage using different definitions was developed and tested on sensors with various surface areas and thicknesses.

Furthermore, the temperature dependence of the leakage current in irradiated sensors has been analysed, which showed that the measured dependence matches the theoretical expectation. The theoretical dependence was used to scale currents from the measurement temperature to another temperature. Lastly, the absolute leakage current was analysed for sensors that were irradiated with different fluences and after different times of annealing, which showed that the measured leakage current roughly matches the theoretical expectation that the leakage current is proportional to the fluence.

Contents

1. Introduction	1
2. The Standard Model of Particle Physics	3
2.1. Fermions	3
2.2. Bosons	4
2.3. Limits of the Standard Model	4
3. The Large Hadron Collider and the ATLAS Experiment	5
3.1. The ATLAS Detector	5
3.1.1. Inner Detector	5
3.1.2. Calorimeters	6
3.1.3. Muon Chambers	6
3.2. The High-Luminosity LHC Upgrade	6
4. Silicon Particle Detectors	9
4.1. Energy Loss of Particles	9
4.2. pn-Diode	9
4.3. Radiation Damage	10
4.3.1. Annealing	11
4.4. Pixel Detectors in the Inner Tracker	11
5. Characterisation of Silicon Pixel Sensors	13
5.1. Planar Sensor Market Survey	13
5.2. Experimental Setup	13
5.3. Measurement of the Leakage Current	13
5.4. Measurement of the Capacitance	15
6. Determining the Depletion Voltage	17
6.1. The Algorithm	17
6.2. Results	19
6.3. Evaluating the Systematic Uncertainties	20

Contents

6.4. Conclusion	22
7. Determining the Breakdown Voltage	23
7.1. The Algorithm	23
7.2. Testing the Algorithm	24
7.3. Conclusion	28
8. Fluence Dependence of the Leakage Current in Irradiated Sensors	31
8.1. Leakage Current for Different Fluences	31
8.2. Leakage Current for Different Annealing Periods	33
9. Relative Temperature Dependence of the Leakage Current in Irradiated Sensors	35
9.1. Testing the Relative Temperature Dependence	35
9.1.1. Results: Climate Chamber	36
9.1.2. Results: Probe Station	40
9.1.3. Comparison of the Results from the Climate Chamber and the Probe Station	43
9.2. Scaling IV Curves to a Reference Temperature	44
10. Summary	47
A. Algorithm to Determine the Depletion Voltage	49
B. Algorithm to Determine the Breakdown Voltage	55

1. Introduction

Today our best theory describing elementary particles and three of the four fundamental forces is the Standard Model (SM), explained in Chapter 2. However, there are phenomena that cannot be described within the SM or even violate its predictions. The goal of particle physics is to improve our understanding and fill the gaps of this theory.

In the search for physics beyond the SM and the refinement of our current knowledge, the experiments at the Large Hadron Collider (LHC), described in Chapter 3, are the most promising as the LHC is the biggest particle collider with the largest achieved energy in the world. In 2012, two of the experiments at the LHC, the ATLAS experiment, described in Section 3.1, and the CMS experiment, discovered the long predicted Higgs boson [1], [2], which filled a big gap in the SM.

For this decade, a high-luminosity upgrade of the LHC is planned to increase the amount of data that is taken and possibly find new physics. For this purpose the detectors will also be upgraded. In the ATLAS experiment, a completely new full-Silicon tracking detector will be installed. The elements of this detector have gone through years of development and are now entering the phase of prototyping and production. The testing of sensors provided by various vendors for the ongoing market survey in order to come to a decision for the tendering and procurement process for the Silicon pixel detectors will be the focus of this thesis.

2. The Standard Model of Particle Physics

So far, the SM is our best theory of matter and its interactions on the atomic and sub-atomic level. The SM includes all the known forces - except for gravity - and makes precise calculations and predictions possible. It contains 12 fermions and their antiparticles (with the same mass but inverse charge, for neutrinos opposite helicity) and five bosons (see Figure 2.1).

2.1. Fermions

Fermions are particles with half-integer spin which make up the known matter in our universe. In the SM there are two kinds: Leptons and quarks.

Leptons can either be electrically charged - with charge $-1e$ - or neutral. Both types come in three generations with electron, muon and tau being the charged ones and the corresponding neutrinos being the neutral ones. Within a family of particles, the mass grows with increasing generation.

Quarks also come in two types with three generations each. There are three up-type quarks (up, charm, top) with electrical charge $2/3e$ and three down-type quarks (down, strange, bottom) with electrical charge $-1/3e$. Quarks additionally have a colour charge, namely red, blue and green, which makes them couple to the strong force.

	Quarks			Gauge Bosons	
mass →	2.4 MeV	1.27 GeV	171.2 GeV	0	~125 GeV
charge →	2/3	2/3	2/3	0	0
spin →	1/2	1/2	1/2	1	0
name →	u up	c charm	t top	γ photon	H Higgs boson
	4.8 MeV	104 MeV	4.2 GeV	0	
	-1/3	-1/3	-1/3	0	
	1/2	1/2	1/2	1	
	d down	s strange	b bottom	g gluon	
	<2.2 eV	<0.17 MeV	15.5 MeV	0	91.2 GeV
	0	0	0	0	0
	1/2	1/2	1/2	1	1
	ν_e electron-neutrino	ν_μ muon-neutrino	ν_τ tau-neutrino	Z⁰ Z boson	
	0.511 MeV	105.7 MeV	1.777 GeV	80.4 GeV	
	-1	-1	-1	±1	
	1/2	1/2	1/2	1	
	e electron	μ muon	τ tau	W[±] W boson	
	Leptons				

Figure 2.1.: Overview of the particles in the Standard Model.

2.2. Bosons

In contrast to the fermions, bosons have an integer spin. Spin-1 bosons are the carriers of three of the four fundamental forces: the electromagnetic interaction, the weak interaction and the strong interaction. The fourth fundamental force, gravity, is ignored in particle physics as its influence is negligible on the mass scale of elementary particles and because there is no way yet to quantise General Relativity.

The carrier boson of the electromagnetic interaction is the photon (γ), which has no mass and hence always moves at the speed of light. The photon couples to all particles with an electric charge.

The carrier bosons of the weak interaction are the W^\pm - and the Z^0 -bosons which couple to the hypercharge of a particle and therefore interact with every known fermion. The weak interaction is weak only for light particles as the carrier bosons have masses themselves ($m_W \approx 80 \text{ GeV}$, $m_Z \approx 90 \text{ GeV}$) and therefore must be virtual in a decay of much lighter fermions.

The last fundamental force is the strong interaction. Its carrier boson is the gluon, which has no mass and couples to fermions with colour charge, thus only to quarks. Gluons also carry colour charges, which makes it possible for them to couple to each other. Another special feature of the strong interaction is a property called confinement which allows only colourless bound states to exist. These bound states are called hadrons.

In addition, there is a spin-0 boson called the Higgs boson. It is an excitation of the Higgs field and gives mass to the particles - therefore it couples to every fermion and the massive bosons.

2.3. Limits of the Standard Model

Although the SM combines most of what we know about matter and fundamental forces, there are several other phenomena that it cannot explain. I will just mention two of them.

- **Dark Matter and Dark Energy:** From the observation of galaxies we know that the actual mass of a galaxy is much larger than what we can detect. Furthermore, observations show that the universe is expanding with increasing speed, which can only be explained by an energy that has not been detected yet.
- **Asymmetry in matter/antimatter distribution:** The SM does describe a matter-antimatter asymmetry via a complex term in the CKM matrix. However, it is not able to describe an asymmetry at the level observed.

3. The Large Hadron Collider and the ATLAS Experiment

The Large Hadron Collider (LHC) [3] at the European Organisation for Nuclear Research CERN in Geneva is the largest synchrotron providing the most powerful colliding beams in the world.

The LHC was built inside a 26.7 km long underground ring tunnel. The accelerator consists of two adjacent beam pipes in which two particle beams are accelerated in opposite directions. The particles that are accelerated are protons or Lead ions and can currently reach an energy of 13 TeV in the center-of-mass system. The beams are focused by magnetic fields and collided in intervals of 25 ns at four interaction points where the beam pipes intersect. Located at these points are the four detectors of the LHC. One of them is ATLAS (**A** Toroidal LHC Apparatu**S**) [4].

3.1. The ATLAS Detector

The ATLAS detector is a general purpose detector and the largest detector at the LHC. It is about 44 m long, 25 m high and covers nearly the full angle around the collision point. It is shown in Figure 3.1. ATLAS consists of several different detectors that are arranged in layers around the beam pipe. Each layer fulfils a different purpose.

3.1.1. Inner Detector

The Inner Detector (ID) is designed to measure the direction, track, momentum, vertices and charge of charged particles, while maintaining most of their energy. It consists of Silicon pixel and strip detectors and a gaseous transition radiation tracker inside a magnetic solenoid field. The pixel detectors are arranged in four barrel layers around the collision point and three disks in each end cap. The strip detector consists of four barrel layers which enclose the pixel layers and 18 end cap discs.

3. The Large Hadron Collider and the ATLAS Experiment

3.1.2. Calorimeters

The ID is enclosed by the electromagnetic and the hadronic calorimeters which measure the deposited energy of particles flying through and ideally stop them completely. Both of them are sampling calorimeters, meaning that passive absorber material and active detector material are arranged in alternating layers.

Directly around the ID is the electromagnetic (EM) calorimeter. Here, mostly electrons and photons deposit their energy. Like the tracking detector, the EM calorimeter consists of a barrel part, surrounding the collision point and an end cap part at each end of the detector. The active material in the EM calorimeter is liquid Argon, the passive material is Lead.

The EM calorimeter is surrounded by the hadronic calorimeter. Its barrel part consists of steel as the absorber material and tiles from plastic scintillators as the active material. The end caps of the hadronic calorimeters are made of Copper and liquid Argon. Both parts are about ten interaction lengths thick, so most high energy hadrons deposit all of their energy in the calorimeter.

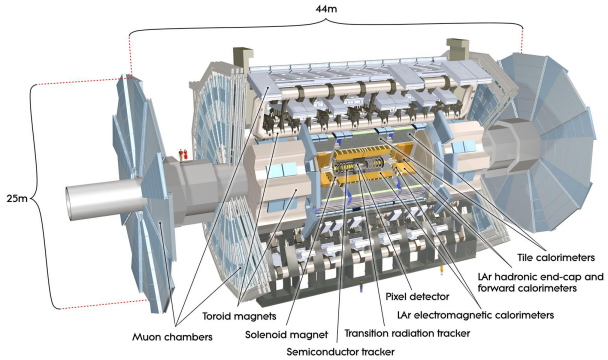


Figure 3.1.: Schematic view of the ATLAS detector. ©CERN

3.1.3. Muon Chambers

As muons are typically minimum ionising particles with a low energy loss through Bremsstrahlung, they mostly pass through the EM and the hadronic calorimeter. To detect them and measure their momentum, ATLAS has a muon detector on the outermost part, mostly consisting of gas filled drift tubes. These muon chambers are located inside a toroidal magnetic field, which is perpendicular to the solenoid field in the inner part of the detector.

3.2. The High-Luminosity LHC Upgrade

In 2018, an instantaneous luminosity of $2 \times 10^{34} \text{ cm}^{-2} \text{ s}^{-1}$ was reached (twice the design value). A total integrated luminosity of 190 fb^{-1} has been collected so far. The High-Luminosity Large Hadron Collider (HL-LHC) project aims at increasing the instantaneous

3.2. *The High-Luminosity LHC Upgrade*

luminosity to $5 - 7.5 \times 10^{34} \text{ cm}^{-2}\text{s}^{-1}$ and collecting in total 4000 fb^{-1} to make more precise measurements of known physics processes or properties, such as the properties of the Higgs boson, and to improve the sensitivity for the search of physics beyond the SM. The upgrade is planned to be finished in 2027. An upgrade of the detectors is necessary to cope with the new conditions, such as the higher pile-up of up to 200 interactions per bunch crossing and the higher radiation level. To keep up with it, the inner detector of ATLAS will be replaced with a new full-Silicon inner tracker (ITk), which has a higher segmentation and is more resistant to radiation damage.

4. Silicon Particle Detectors

Pure Silicon forms dense crystals where the energy levels of the atoms are so close together that they can be described with bands. Electrons in the valence band are mostly stationary at their atoms while electrons in the conduction band can move freely through the lattice. The gap between these bands is about 1.12 eV, which makes Silicon a semiconductor.

4.1. Energy Loss of Particles

In Silicon detectors only charged particles and photons are detectable. Charged particles lose their energy via ionisation, while photons mainly interact with the material via the photoelectric effect. In both cases electrons from the valence band are excited to the conduction band, creating electrons and holes, which act as mobile charge carriers.

4.2. pn-Diode

A Silicon detector is made of pn-diodes. It is a junction of two differently doped Silicon materials as shown in Figure 4.1. Doping with donors creates an n-type material and doping with acceptors creates a p-type material. The mobile charges created by the additional or missing valence electron of the dopant diffuse and recombine at the border of two different types. The ions left behind create a zone of stationary charges resulting in an electric field. This is the depletion zone and it can be broadened or shrunk by applying a reverse or forward voltage, respectively. The reverse bias voltage V needed to create a depletion zone of depth w can be calculated by

$$w = \sqrt{\frac{2\epsilon_0\epsilon_r V}{eN_{\text{eff}}}}, \quad (4.1)$$

with the effective dopant concentration N_{eff} , the elementary charge e , the dielectric constant of the vacuum ϵ_0 and the relative permittivity of Silicon ϵ_r . The depletion voltage is defined by the voltage at which the sensor is fully depleted ($w = d$, with d - thickness

4. Silicon Particle Detectors

of the sensor). It can be calculated with

$$V_{\text{dep}} = \frac{d^2 \cdot e N_{\text{eff}}}{2\epsilon_0\epsilon_r}. \quad (4.2)$$

The capacitance of a pn-junction is also dependent on the depletion depth and thus on the voltage as

$$C = A \frac{\epsilon_0\epsilon_r}{w} = A \sqrt{\frac{\epsilon_0\epsilon_r \cdot e N_{\text{eff}}}{2V}}, \quad (4.3)$$

with the area of the sensor A . The goal is to measure an ionisation current and therefore a fully depleted detector and a low level of leakage current is needed. The leakage current in the depleted Silicon bulk is generated by thermal excitation and scales with temperature as:

$$I_{\text{leak}} \propto T^2 \exp\left(-\frac{E_G}{2kT}\right), \quad (4.4)$$

with the temperature T , the effective band gap E_G and the Boltzmann-constant k .

4.3. Radiation Damage

Radiation can damage the Silicon crystal and thereby create new energy levels inside the band gap. This can change the effective doping concentration, which increases the required voltage for a full depletion. It can also cause signal charges to be trapped temporarily. Moreover, it leads to an increase of the leakage current as [5]:

$$\Delta I_{\text{leak}} = \alpha V \Phi_{\text{eq}}, \quad (4.5)$$

with the volume of the detector V , the radiation damage rate α and the 1-MeV-neutron equivalent fluence Φ_{eq} .

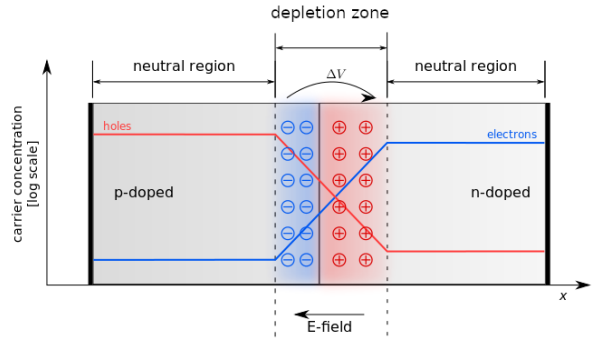


Figure 4.1.: Sketch of a pn-junction with stationary charges in the depletion zone.

4.3.1. Annealing

When a Silicon sensor rests at a high enough temperature, defects that were inflicted by irradiation can self repair. This process is called annealing. Depending on the duration and the temperature of the annealing process, the leakage current caused by irradiation can decrease. This can be expressed in a dependence of the current related radiation damage rate $\alpha(t_{\text{ann}}, T_{\text{ann}})$ [5] where t_{ann} is the annealing time and T_{ann} the annealing temperature.

4.4. Pixel Detectors in the Inner Tracker

The new inner tracking detector (ITk) [6] for the ATLAS detector is planned to be installed to cope with the challenges resulting from the HL-LHC upgrade, in particular higher occupancy and radiation levels in the order of $10^{16} \text{ n}_{\text{eq}}\text{cm}^{-2}$. There will be a cylindrical detector with five radial layers of pixel detectors (numbered L0 - L4) and four layers of strip detectors, in addition to end-caps. In this work, the focus will be on the pixel detectors.

The detectors that will be installed are hybrid pixel detectors. This means that the sensor itself is bump-bonded to a read out chip. The innermost layer (at only 3.4 cm distance from the beam) will consist of $150 \mu\text{m}$ thick 3D sensors with a pixel size of $25 \times 100 \mu\text{m}^2$ in the barrel part and $50 \times 50 \mu\text{m}^2$ in the end-cap part. Despite the higher production cost, this choice was made because in 3D detectors the distance between the vertical electrodes is significantly smaller than in planar detectors, which makes them less susceptible to trapping of charges and thus radiation harder.

In L1, planar sensors with a thickness of $100 \mu\text{m}$ and a pixel size of $50 \times 50 \mu\text{m}^2$ will be installed. Compared to the planar sensors in layer L2-L4 with a thickness of $150 \mu\text{m}$ and sizes of $50 \times 50 \mu\text{m}^2$ and $100 \times 25 \mu\text{m}^2$ they are radiation harder but also give a lower signal. The whole detector is made of n-in-p sensors to reduce trapping and avoid inversion of the doping type.

While the outer three layers of the ITk pixel detector are designed to operate for the full HL-LHC data taking period, the inner two layers of the detector will be replaced after half of the lifetime.

5. Characterisation of Silicon Pixel Sensors

5.1. Planar Sensor Market Survey

To ensure that the produced sensors meet the ITk specifications, a market survey is carried out. Single and double chip sensors compatible with the RD53A prototype readout chip [7] produced by various vendors are tested. A visual inspection is made and thickness and planarity of the sensors are measured. Furthermore, the leakage current is measured over time (I_t) and as a function of the applied voltage (IV). The capacitance and the depletion voltage is measured via the capacitance-voltage characteristics (CV). In this thesis, the focus is placed on the analysis of IV and CV measurements of sensors from two different vendors (called Foundry 3 and Foundry 4 in the following).

5.2. Experimental Setup

For characterisation of the sensors mostly two setups are used: a temperature controlled semi-automatic probe station, as shown in Figure 5.1, for bare sensor measurements and a climate chamber for measuring sensors mounted on a PCB (printed circuit board) at a controlled temperature.

The voltage ranges and steps at which I_{leak} and C are measured are listed in Table 5.1, as well as the number of averaged measurements and the wait time in between the measurements. Both measurements are aborted at $I_{\text{leak}} = 10 \mu\text{A}$ when unirradiated sensors are measured and at $I_{\text{leak}} = 100 \mu\text{A}$ when measuring irradiated sensors.

5.3. Measurement of the Leakage Current

The leakage current of an ideal sensor is expected to be constant beyond the depletion voltage as it scales with the volume of the depletion zone. However, in real detectors it can increase further, due to surface and edge current. Example IV curves of sensors without

5. Characterisation of Silicon Pixel Sensors

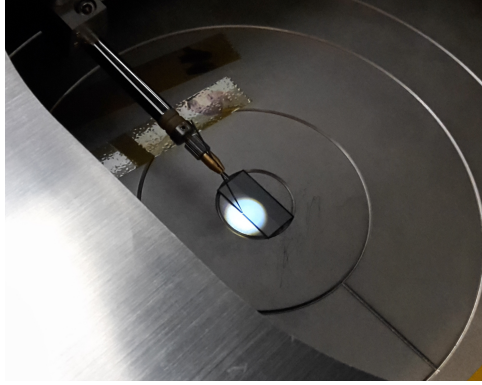


Figure 5.1.: A pixel sensor placed on a probe station.

	IV	CV
steps	5 V	5 V
range	0 – 600 V	0 – 200 V
averages	10	5
wait time	10 s	5 s

Table 5.1.: Measuring specifications of IV and CV measurements.

a breakdown in the range 0 – 600 V are compared to the IV curve of an ideal sensor in Figure 5.2. These measurements were made on the probe station and the fluctuations of the curves are caused by the chiller cycle (see Section 9.1.2). Other example sensor measurements, shown in Figure 5.3, have a breakdown, where the leakage current grows rapidly beyond a certain voltage, called breakdown voltage. The sensors in both examples are unirradiated.

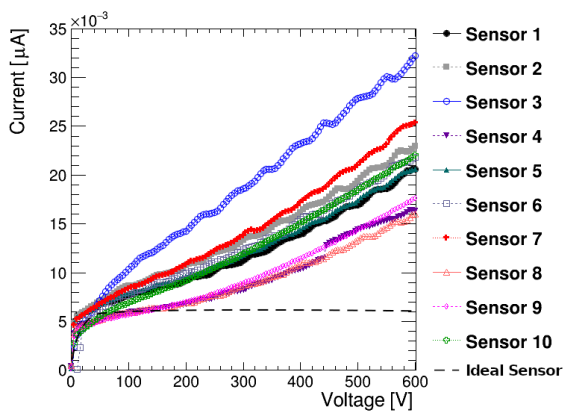


Figure 5.2.: Measured IV curves without a breakdown compared to an ideal IV behaviour.

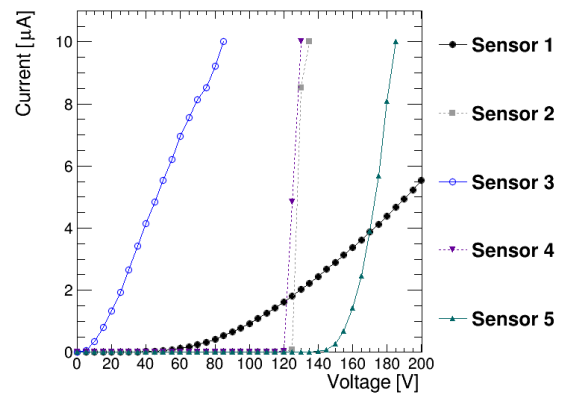


Figure 5.3.: Measured IV curves with a breakdown.

Additionally, the IV behaviour is measured at different temperatures and after the sensors have been irradiated to evaluate their radiation hardness.

5.4. Measurement of the Capacitance

In Figure 5.4, $\frac{1}{C^2}$ is plotted against the applied voltage. Finding the point where C becomes constant gives the voltage needed for a full depletion (see Equation 4.3). For that purpose, straight lines can be fitted to the increasing and the constant part of $\frac{1}{C^2}(V)$ and their intersection is calculated. With Equation 4.3 it is also possible to derive the effective doping concentration from the slope of the increase of $\frac{1}{C^2}$.

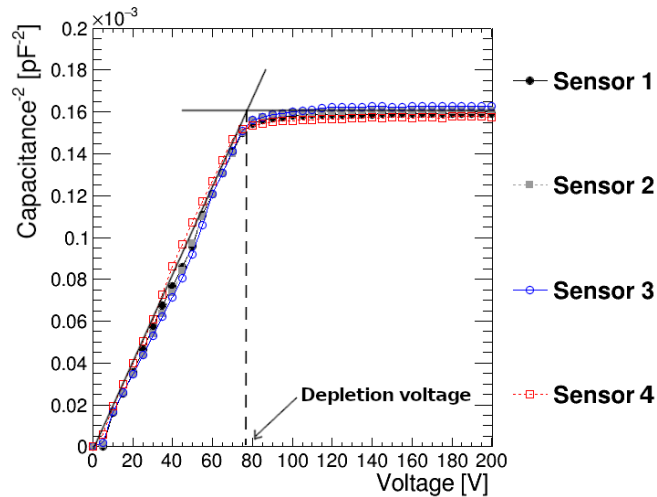


Figure 5.4.: CV curves for sensors with $V_{\text{dep}} \approx 76$ V. The straight lines illustrate possible fits to determine the depletion voltage.

6. Determining the Depletion Voltage

In Section 5.4, it is described how the depletion voltage of a Silicon sensor can be determined from the capacitance measurement. This chapter is about developing an algorithm that automates the process as much as possible. The code of the algorithm can be found in appendix A.

6.1. The Algorithm

Two methods were developed to find the depletion voltage from the CV curves. In both methods a function is fitted to the measured CV curve, using the χ^2 -fitting-tool in ROOT. In a first step, a pre-fit is done that initialises the fit parameters for the final fit. This pre-fit is the same for both methods.

Pre-Fit

In the pre-fit, a straight line ($f_{\text{slope}}(V)$) is fitted to a part of the sloped section and a constant straight line ($f_{\text{const}}(V)$) is fitted to a part of the constant section of the CV curve. The functions used for that are

$$f_{\text{slope}}(V) = aV + b \quad \text{and} \quad f_{\text{const}}(V) = c$$

and the fit parameters are a , b and c .

The sections to which these functions are fitted are given with the parameters `slopeBegin`, `slopeEnd`, `constBegin` and `constEnd`. f_{slope} is fitted in the voltage range from `slopeBegin` to `slopeEnd` and f_{const} is fitted in the voltage range from `constBegin` to `constEnd`. For these parameters, default values are defined in the function but they can also be set manually. A visualisation of the pre-fit and these parameters is shown in Figure 6.1. By default, `slopeBegin` and `slopeEnd` are defined to skip the first two points of the measurement and range over six points. The default values of `constBegin` and `constEnd` skip the last two

6. Determining the Depletion Voltage

points of the measurement and also ranges over 6 points. The first and last two points of the measurement are skipped as they occasionally deviate from the expected behaviour and therefore disturb the fit.

When both functions are fitted to the measurement, the voltage of their intersection is calculated, which gives a first approximation for the depletion voltage $V_{\text{dep,approx}}$.

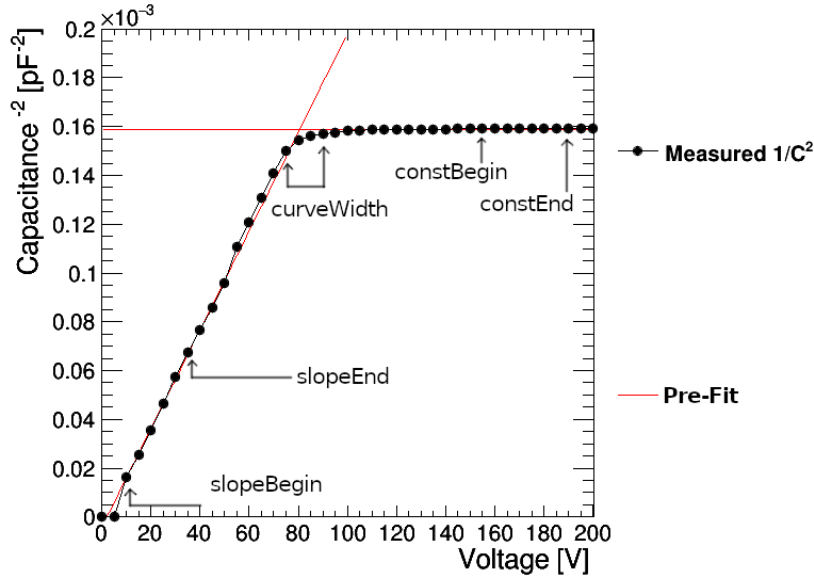


Figure 6.1.: Pre-fit to the CV curve of single chip sensor 1 from Foundry 4.

Final Fit

Method 1

The final fit of method 1 is very similar to the pre-fit. Again, two straight lines are fitted to the measured CV curves. The functions that describe them are

$$g_{\text{slope}}(V) = a_f V + b_f \quad \text{and} \quad g_{\text{const}}(V) = c_f.$$

The fit parameters (a_f, b_f, c_f) are initialised with the results of the fit parameters (a, b, c) from the pre-fit. However, the sections to which the straight lines are fitted are different. The sloped straight line is fitted from `slopeBegin` to $V_{\text{dep,approx}} - \text{curveWidth}/2$ and the constant line is fitted from $V_{\text{dep,approx}} + \text{curveWidth}/2$ to `constEnd`. This way, the curved section of the CV curve, which does not match the simple theoretical model, is left out of the fit. `curveWidth` can be set manually or left as default. The default value of `curveWidth` is set to be equal to the voltage covered by three measurement points.

The final value for V_{dep} is then determined by calculating the voltage at which both straight lines intersect.

Method 2

For the second method a continuous function was built, which is a sloped straight line for voltages lower than V_{dep} and a constant for voltages higher than V_{dep} . The pseudo code for that function is shown below. Both sections of the function can be described similar to the functions used in method 1, only the y-intercept is changed to be dependent on the slope, the constant and V_{dep} to make the function continuous and use V_{dep} as a fit parameter.

```
myfunction(voltage,  $V_{\text{dep}}$ , slope, const)
  if(voltage <  $V_{\text{dep}}$ ): return voltage·slope+(constant-slope· $V_{\text{dep}}$ )
  else: return const
```

The fit parameters (V_{dep} , slope, const) are initialised to the results of the pre-fit ($V_{\text{dep,approx}}$, a , c) and the function is then fitted to the CV curve in the range from slopeBegin to constEnd. The advantage of this method is that V_{dep} is a direct fit parameter, the disadvantage is that the function is also fitted to the curved section, which is not included in the theoretical model and could potentially disturb the fit.

6.2. Results

Both methods were tested on the CV curves of four single chip (SC) sensors from Foundry 4. The results are shown in Table 6.1 (errors are calculated from the statistical fit errors). An example of both methods being applied to the CV curve of sensor 1 is shown in Figure 6.2.

Sensor	$V_{\text{dep}}[\text{V}]$	
	Method 1	Method 2
Sensor 1	79.60 ± 0.05	80.30 ± 0.03
Sensor 2	83.45 ± 0.03	83.17 ± 0.02
Sensor 3	83.91 ± 0.03	83.80 ± 0.02
Sensor 4	74.04 ± 0.07	73.54 ± 0.03

Table 6.1.: Determined depletion voltages for SC sensors from Foundry 4.

6. Determining the Depletion Voltage

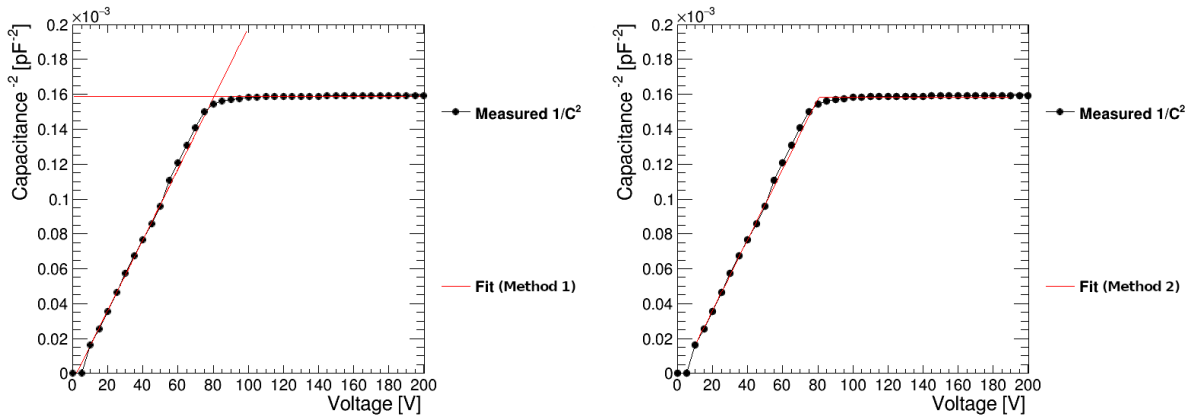


Figure 6.2.: CV curves of SC sensor 1 from Foundry 4 and the fitted function from method 1 (left) and method 2 (right).

Both methods give similar results that agree with the CV behaviour of the sensors that were tested. However, the results are still sensitive to the set values of `slopeBegin`, `constEnd` and `curveWidth` (only method 1). The systematic uncertainties, introduced by this, are evaluated in the following.

6.3. Evaluating the Systematic Uncertainties

Method 1

The results for V_{dep} of sensor 1 (Foundry 4) determined by method 1 for different values of `slopeBegin`, `constEnd` and `curveWidth` are shown in Table 6.2 (while one parameter is changed, the other two are held at their default values).

It can be seen that the result of method 1 changes when any of the parameters is varied. The result changes the most when the beginning of the fitting range is varied and when `slopeBegin` comes close to the curved section, the statistical fit error increases drastically. However, the dependence on `curveWidth` is most interesting as `slopeBegin` and `constEnd` can be kept at default for most CV curves. For the values of `curveWidth` that were tested the resulting depletion voltage stays within a 0.81 V interval. This means that for CV curves with a wider or narrower curved section than 10 V, the default value of `curveWidth` should still work fine.

In the (rather large) ranges of the parameters, for which method 1 was tested, most of the results are located in an interval between 78.0 V and 80.5 V, so the systematic uncertainty of V_{dep} can be estimated to be approximately 1.4 V (deviation from the mean at 79.1 V).

slopeBegin [V]	V_{dep} [V]	curveWidth [V]	V_{dep} [V]
10 ←-default	79.60 ± 0.05	0	80.27 ± 0.04
20	78.85 ± 0.08	10 ←-default	79.60 ± 0.05
30	78.3 ± 0.2	20	79.68 ± 0.05
40	75.8 ± 0.3	30	79.81 ± 0.05
50	78.0 ± 0.7	40	79.90 ± 0.05
60	79 ± 3	50	79.92 ± 0.05
		60	80.41 ± 0.06
constEnd [V]	V_{dep} [V]		
190←-default	79.60 ± 0.05		
170	79.53 ± 0.05		
150	79.43 ± 0.05		
130	79.18 ± 0.06		
110	78.89 ± 0.06		
90	78.50 ± 0.07		

Table 6.2.: Results for V_{dep} of sensor 1 (Foundry 4) determined by method 1 with different values for `slopeBegin`, `constEnd` and `curveWidth`.

Method 2

The results for V_{dep} of sensor 1 (Foundry 4) determined by method 2 for different values of `slopeBegin` and `constEnd` are shown in Table 6.3 (while one parameter is changed, the other one is held at its default value).

The results of method 2 shows a slightly stronger dependence on the parameters `slopeBegin` and `constEnd` than the results of method 1. Here, most results are in an interval between 77.7 V and 81.6 V, so the systematic uncertainty of V_{dep} can be estimated to be 2.4 V (deviation from the mean at 79.2 V).

6. Determining the Depletion Voltage

<code>slopeBegin</code> [V]	V_{dep} [V]	<code>constEnd</code> [V]	V_{dep} [V]
10 \rightarrow default	80.30 ± 0.03	190 \rightarrow default	80.30 ± 0.03
20	78.39 ± 0.03	170	80.21 ± 0.03
30	77.97 ± 0.04	150	80.10 ± 0.03
40	76.72 ± 0.04	130	78.30 ± 0.03
50	81.60 ± 0.04	110	77.99 ± 0.03
60	82.23 ± 0.05	90	77.72 ± 0.03

Table 6.3.: Results for V_{dep} of sensor 1 (Foundry 4) determined by method 2 with different values for `slopeBegin` and `constEnd` .

6.4. Conclusion

Both methods give similar results for the depletion voltage and have relatively low statistical and systematic uncertainties at the default settings of the parameters. Method 1 is slightly more stable when changing the fitting range, but overall both methods can be used as fully automatic algorithms to determine the depletion voltage from CV curves with the default parameters.

7. Determining the Breakdown Voltage

The breakdown voltage V_{BD} is the reverse bias voltage at which the leakage current in a Silicon sensor increases rapidly, mainly due to charge avalanches. This chapter describes the process of developing an algorithm, which can detect a breakdown in an IV curve of an unirradiated sensor and determines the breakdown voltage. The code of this algorithm can be found in appendix B.

There are different definitions in ITk documents¹ of where the breakdown voltage can be located, if a breakdown is detected. Three of them are stated below. All definitions are only valid for unirradiated sensors and at voltages above the depletion voltage as the increase in leakage current at voltages below V_{dep} is due to the widening depletion zone and shall not be mistaken for a breakdown. In reality, a breakdown can also occur below V_{dep} , for these cases other methods were implemented, which will be shown later.

Definition 1: If the leakage current increases more than 20% within a 5 V step, the voltage at the start of that step is the breakdown voltage.

Definition 2: If the leakage current increases faster than a certain slope, the voltage before that slope is exceeded is the breakdown voltage.

Definition 3: If the leakage current increases more than 100% within a 5 V step, the voltage which is 5 V lower than the voltage at the start of that step is the breakdown voltage.

7.1. The Algorithm

The algorithm that was developed scans the measurement points of an IV curve, starting at the depletion voltage, and tests whether and at what voltage the criterion for a breakdown from the selected definition is met. The selection of the criteria is made by calling the function with an option. When called with option 1, 2 or 3, the algorithm tests for the definitions 1, 2 or 3 stated above, respectively.

¹ATLAS-internal communication.

7. Determining the Breakdown Voltage

Testing revealed that none of these definitions reliably determine if a breakdown occurs (see Section 7.2), so another criterion for a breakdown was added: Calling the function with option 4 gives back the voltage where a certain current threshold is crossed, regardless whether this voltage is lower than the depletion voltage or not. This option is not expected to determine the breakdown voltage, but is implemented to test the existence of a breakdown. Additionally, a functionality (option 5) was added, for which the algorithm first runs option 4 and then searches for the lowest voltage, where definition 2 is met, starting from the result of option 4.

The pseudo code of the function is shown below.

```
findVBD(graph, depVoltage, option, slopeDefine, threshold)
  Go through points of graph
  if(option = "option1" & voltage > depVoltage)
    if( $I_{leak}(voltage+5)/I_{leak}(voltage) > 1.2$ )
      return voltage
  if(option = "option2" & voltage > depVoltage)
    if( $(I_{leak}(voltage+5V)-I_{leak}(voltage))/5V > slopeDefine$ )
      return voltage
  if(option = "option3" & voltage > depVoltage)
    if( $I_{leak}(voltage+10V)/I_{leak}(voltage+5V) > 2$ )
      return voltage
  if(option = "option4")
    if( $I_{leak}(voltage) > threshold$ )
      return voltage
  if(option = "option5")
    Go through points of graph from voltage = findVBD(graph, depVoltage,
    "option4", slopeDefine, threshold) backwards
    if( $(I_{leak}(voltage)-I_{leak}(voltage-5V))/5V < slopeDefine$ )
      return voltage
```

7.2. Testing the Algorithm

The algorithm was tested on IV measurements of 32 single chip (SC), 20 double chip (DC) and 6 quad chip (QC) sensors from Foundry 3 and 10 SC and 20 DC sensors from Foundry 4.

The value of `slopeDefine` is set to 4 nA/V (SC), 8 nA/V (DC), 16 nA/V (QC). The

value of `threshold` is chosen to be equal to the ITk-specification $I_{\text{leak}} \stackrel{!}{<} 0.75 \mu\text{A}/\text{cm}^2$ (`threshold` = 1.4 μA (SC), 2.9 μA (DC), 5.8 μA (QC)). `depVoltage` is 40 V for the sensors from Foundry 3 and 80 V for the sensors from Foundry 4.

The resulting breakdown voltages, determined using the different options, are recorded in Tables 7.1 and 7.2. Only the measurements, where the function detected a breakdown with any of the criteria are listed.

Sensor	$V_{\text{BD}}[\text{V}]$				
	Option1	Option2	Option3	Option4	Option5
SC (150 μm)					
S01	45	45	-	120	45
S05	-	45	-	10	0
S06	120	120	115	130	120
S08	-	45	-	25	0
S12	180	185	180	-	-
S13	-	45	-	60	0
S14	115	120	110	125	120
S15	200	-	-	-	-
S16	50	140	135	165	140
SC (100 μm)					
S01	45	45	-	110	45
S03	75	-	-	-	-
S04	-	120	-	-	-
S05	75	-	-	-	-
S08	-	45	-	20	0
S11	60	-	-	-	-
S12	85	-	-	-	-
S14	95	95	90	105	95
S15	-	-	-	5	0
S16	45	45	-	60	20
DC (150 μm)					
S02	-	45	-	-	-
S04	-	120	-	-	-
S06	-	-	-	5	0
S07	-	-	-	15	10

7. Determining the Breakdown Voltage

S10	100	100	95	115	100
DC (100 μm)					
S01	95	95	90	105	95
S03	75	150	145	165	150
S07	75	-	-	-	-
S08	45	45	-	45	5
S09	70	-	-	-	-
S10	-	45	-	70	0
QC (150 μm)					
S01	-	-	-	5	0
S03	-	-	-	20	0
QC (100 μm)					
S01	55	95	-	-	-
S02	-	45	-	5	0

Table 7.1.: Determined breakdown voltages of sensors from Foundry 3 with the different options (sensor thickness in parentheses).

Sensor	$V_{BD}[\text{V}]$				
	Option1	Option2	Option3	Option4	Option5
SC					
S04	530	555	525	-	-
S09	405	460	530	-	-
S10	600	-	-	-	-

Table 7.2.: Determined breakdown voltages of sensors from Foundry 4 with the different options.

The measurements for which all options detect a breakdown and determine a similar breakdown voltage show hard breakdowns, meaning that the current increases rapidly from a previously low value to a value above `threshold`, as seen in the graphs in Figure 7.1.

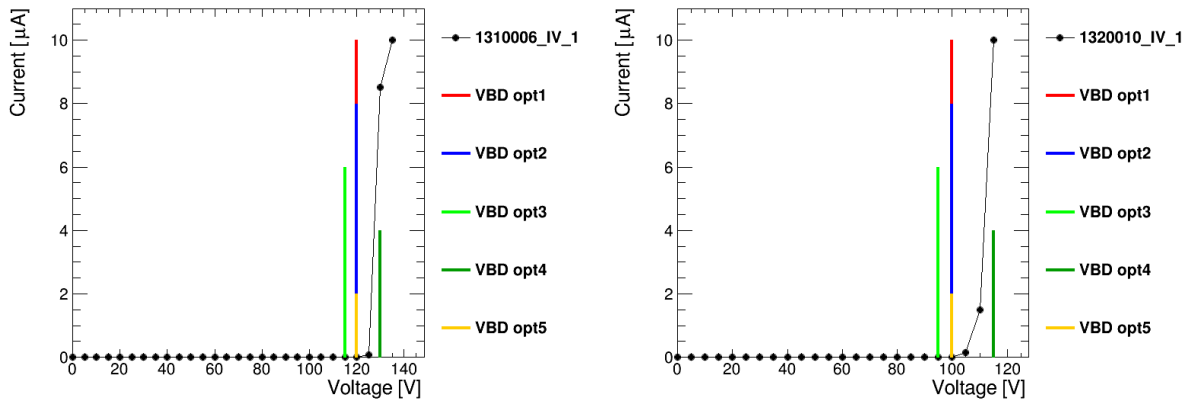


Figure 7.1.: IV curves of 150 μm thick SC sensor 6 (left) and DC sensor 10 (right) from Foundry 3 and the determined breakdown voltage.

In these cases, all definitions give reliable results, however, there are other kinds of breakdowns and IV curves without a breakdown, for which some of the definitions fail.

It is visible that occasionally option 1 recognizes a breakdown, even though `threshold` is not crossed. This can happen if there are leaps in the leakage current, although no breakdown occurs, as shown in the graph of SC sensor 5 (Foundry 3) in Figure 7.2. On the other hand, option 2 and option 3 sometimes do not recognize a breakdown, although there is one. This is the case if the current does not grow abruptly but with an increasing slope (soft breakdown) as in the graph of sensor 4 in Figure 7.2.

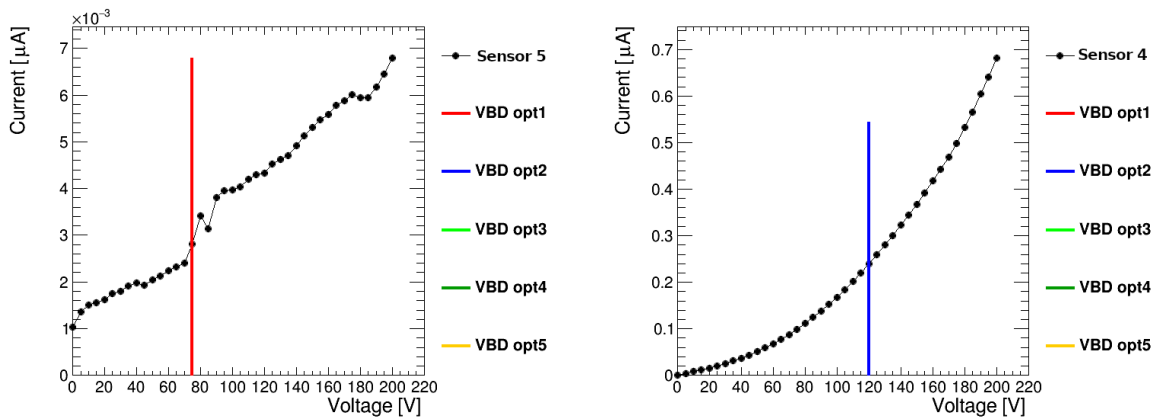


Figure 7.2.: IV curves of 100 μm thick SC sensor 5 (left) and sensor 4 (right) from Foundry 3 and the determined breakdown voltage.

Option 2 is very reliable in all the testing that was done. The only cases in which this option detects a breakdown, although option 4 does not, are measurements where the IV

7. Determining the Breakdown Voltage

curve looks like a breakdown, but the measurement has not been done far enough for `threshold` to be crossed, as in the graph of sensor 4 (Foundry 3) in Figure 7.2. The only weakness of this option is that it can only determine breakdown voltages higher than the depletion voltage. Figure 7.3 shows the measurement of DC sensor 6 (Foundry 3), where `threshold` is crossed below V_{dep} , and the measurement of DC sensor 8 (Foundry 3), where a soft breakdown begins below V_{dep} .

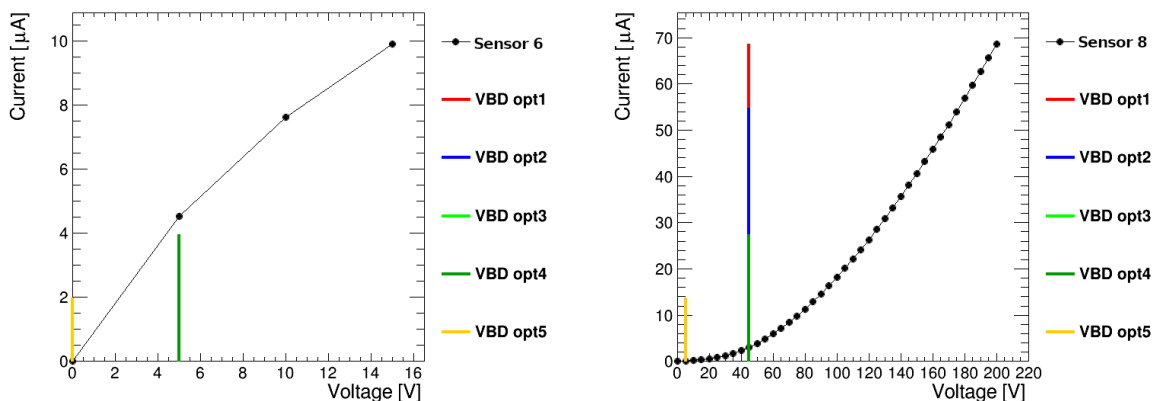


Figure 7.3.: IV curves of 150 μm thick DC sensor 6 (left) and 100 μm thick DC sensor 8 (right) from Foundry 3 and the determined breakdown voltages.

For DC sensor 6 (Foundry 3) option 2 does not detect a breakdown, as the measurement is stopped before V_{dep} . Here, it is not clear whether a breakdown occurs or the current in the sensor is just too high in general. Either way, the sensor does not meet the ITk requirements. For DC sensor 8 (Foundry 3) option 2 detects a breakdown, but the determined breakdown voltage is too high, as the soft breakdown starts below the depletion voltage. In these cases, option 5 is the better option. If the measurement has been made far enough for `threshold` to be crossed, option 5 is always reliably detecting the breakdown voltage.

7.3. Conclusion

Option 2 (searching for the exceedance of a defined slope at voltages higher than V_{dep}) and option 5 (searching for the exceedance of a defined slope backwards from the voltage, at which a certain current threshold is crossed) complement each other in their ability of finding the breakdown voltage. If a measurement of a sensor with a breakdown is not made far enough for `threshold` to be crossed, option 2 can still determine the breakdown

7.3. Conclusion

voltage and if a breakdown occurs at voltages lower than V_{dep} , option 5 can determine the breakdown voltage. Combining both options gives the most reliable method to find V_{BD} .

8. Fluence Dependence of the Leakage Current in Irradiated Sensors

As explained in Section 4.3, the leakage current of a Silicon sensor increases when it is irradiated. In this chapter, IV curves of irradiated sensors from Foundry 3 and 4 are compared to the theoretically expected leakage current, calculated with Equation 4.5. The sensors that are tested were irradiated with 23 MeV protons in Birmingham to fluences of $2 \times 10^{15} \text{ n}_{\text{eq}}/\text{cm}^2$ and $5 \times 10^{15} \text{ n}_{\text{eq}}/\text{cm}^2$ and annealed for 3 days and 10 days. Also, two sensor types were tested, the first type has a thickness of $150 \mu\text{m}$, the second type a thickness of $100 \mu\text{m}$. All of them have a surface area of $2.00 \times 0.96 \text{ cm}^2$.

The current related damage rates $\alpha(t_{\text{ann}})$ used to calculate the theoretical value were taken from [5]. The annealing process took place at room temperature ($\approx 20^\circ\text{C}$) and all compared IV curves were measured or scaled to -25°C . As the leakage current in unirradiated sensors is orders of magnitude smaller than after irradiation, the measured current in irradiated sensors is assumed to be equal to the increase caused by irradiation.

8.1. Leakage Current for Different Fluences

In Figure 8.1 the IV curves of irradiated sensors from Foundry 4 are compared to the theoretical expectation for both fluences mentioned above. All of the sensors were annealed for 10 days and have a thickness of $150 \mu\text{m}$.

8. Fluence Dependence of the Leakage Current in Irradiated Sensors

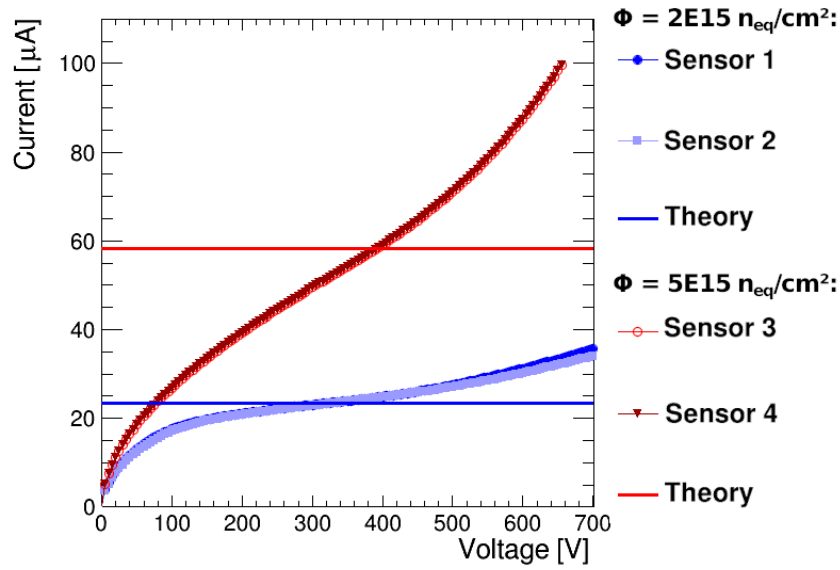


Figure 8.1.: IV curves of irradiated sensors from Foundry 4 compared to the theoretical expectations.

The IV curves of the sensors that were irradiated to the same fluence show a close correspondence. It is clearly visible that the theoretically expected current intersects with the IV curve at some point for both irradiation levels (at ≈ 300 V for $\Phi = 2 \times 10^{15}$ $n_{\text{eq}}/\text{cm}^2$ and at ≈ 400 V for $\Phi = 5 \times 10^{15}$ $n_{\text{eq}}/\text{cm}^2$) and that the increase of leakage current from 2×10^{15} $n_{\text{eq}}/\text{cm}^2$ to 5×10^{15} $n_{\text{eq}}/\text{cm}^2$ is similar to the difference in the theoretical expectations. In contrast to the theoretical expectation, neither of the IV curves show a plateau, but instead the current grows beyond the theoretical expectation, presumably due to charge multiplication and surface and edge contributions. The rate of growth beyond the voltage where the theoretical expectation is met is larger for the sensors which were irradiated to a higher fluence.

Figure 8.2 shows the IV curves of sensors from Foundry 3. Here, two sensors with a thickness of $150 \mu\text{m}$ and four sensors with a thickness of $100 \mu\text{m}$ are compared to the theoretical expectations. All sensors were annealed for 10 days.

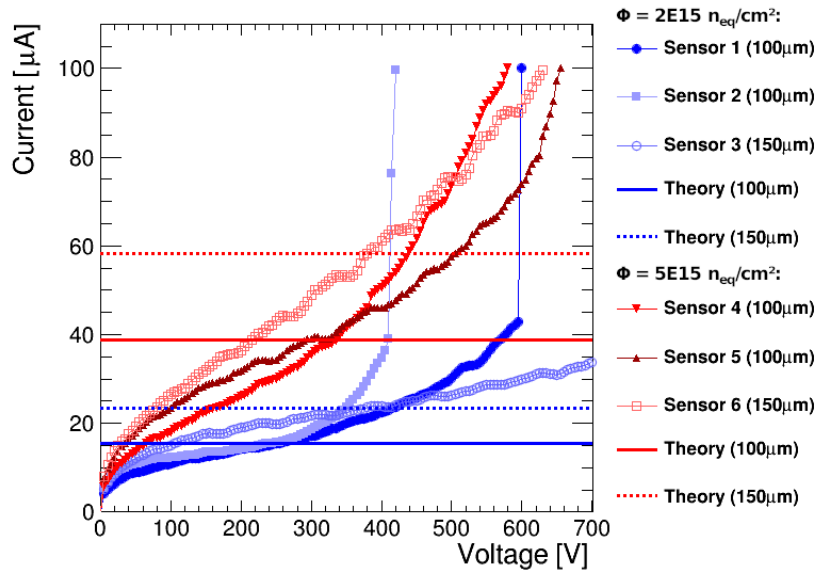


Figure 8.2.: IV curves of irradiated sensors of different thicknesses from Foundry 3 compared to the theoretical expectations (thickness in parentheses).

It is visible that the two thinner sensors irradiated with $2 \times 10^{15} \text{ n}_{\text{eq}}/\text{cm}^2$ show a current breakdown. Again, the measured curves intersect the theoretical expectations (at $\approx 250 \text{ V}$ for $\Phi = 2 \times 10^{15} \text{ n}_{\text{eq}}/\text{cm}^2$ and a thickness of $100 \mu\text{m}$, at $\approx 340 \text{ V}$ for $\Phi = 2 \times 10^{15} \text{ n}_{\text{eq}}/\text{cm}^2$ and a thickness of $150 \mu\text{m}$, at $\approx 320 \text{ V}$ for $\Phi = 5 \times 10^{15} \text{ n}_{\text{eq}}/\text{cm}^2$ and a thickness of $100 \mu\text{m}$ and at $\approx 380 \text{ V}$ for $\Phi = 5 \times 10^{15} \text{ n}_{\text{eq}}/\text{cm}^2$ and a thickness of $150 \mu\text{m}$). The difference between both irradiation levels and both thicknesses roughly match the theory. The correspondence between the IV curves of sensors which were irradiated to the same fluence and have the same thickness is not as close as in the measured sensors from Foundry 4.

8.2. Leakage Current for Different Annealing Periods

In Figure 8.3, the IV curves of sensors from Foundry 4 after 3 days and 10 days of annealing are compared to the theoretical expectation.

8. Fluence Dependence of the Leakage Current in Irradiated Sensors

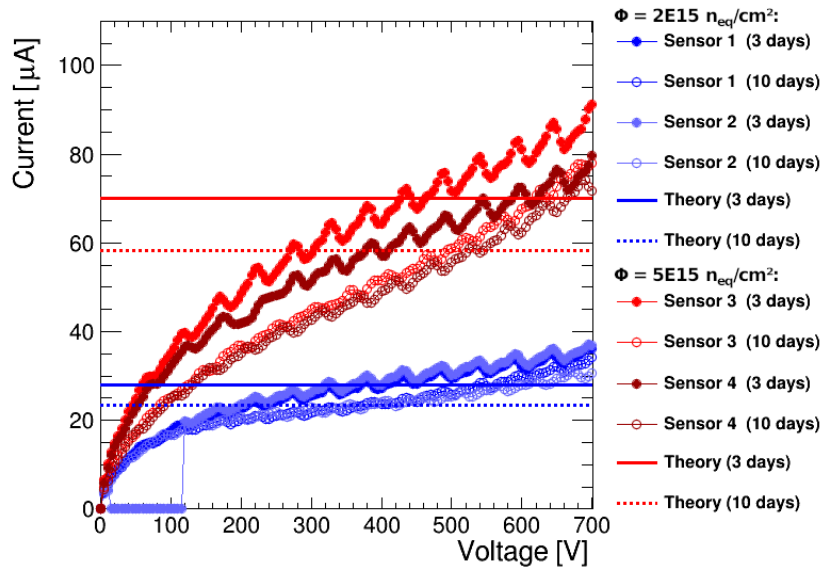


Figure 8.3.: IV curves for sensors from Foundry 4 at different irradiation levels and different annealing periods compared to the theoretical expectation (annealing time in parentheses).

As expected, the leakage current decreases with longer annealing time in all sensors (see Section 4.3.1). The difference between both annealing times is roughly as large as the theory predicts and it is visible that the absolute reduction of the leakage current due to annealing is higher for the sensors which were irradiated with a higher fluence, as expected.

9. Relative Temperature Dependence of the Leakage Current in Irradiated Sensors

This chapter is devoted to the analysis of the temperature dependence of the leakage current in irradiated Silicon sensors. The goal is to compare the dependence that can be inferred from the measurements to the theoretical dependence shown in Equation 4.4. For this purpose, IV curves from irradiated sensors from Foundry 3 and 4, which were measured at different temperatures, are analysed. The sensors were irradiated to fluences of $2 \times 10^{15} \text{ n}_{\text{eq}}/\text{cm}^2$ and $5 \times 10^{15} \text{ n}_{\text{eq}}/\text{cm}^2$.

9.1. Testing the Relative Temperature Dependence

Looking at the IV curves of an irradiated sensor which was measured at different temperatures, it is obvious that the leakage current is strongly temperature dependent (see Figure 9.1).

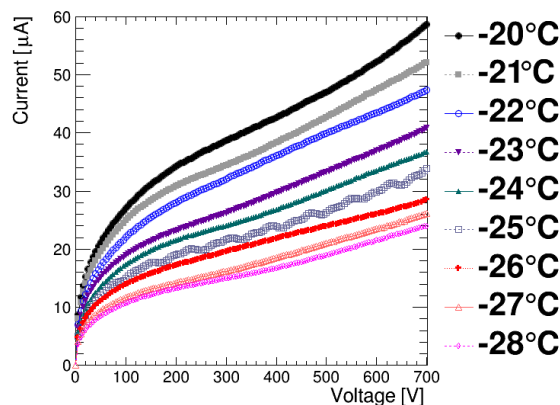


Figure 9.1.: IV curves from an irradiated sensor ($5 \times 10^{15} \text{ n}_{\text{eq}}/\text{cm}^2$) from Foundry 3 measured on the probe station at different temperatures.

9. Relative Temperature Dependence of the Leakage Current in Irradiated Sensors

The relative temperature dependence is evaluated and compared to Equation 4.4. This is done by taking current measurements of an irradiated sensor and calculating the current ratio at different temperatures. If the leakage current obeys Equation 4.4, this ratio should be connected to the temperatures T_1 and T_2 at which these measurements were done as:

$$\frac{I(T_1)}{I(T_2)} = \frac{T_1^2}{T_2^2} \cdot \exp\left(\frac{E_g(T_1 - T_2)}{2kT_1T_2}\right). \quad (9.1)$$

In the following, the current ratio $\frac{I(T_1)}{I(T_2)}$ of sensors measured in the climate chamber and on the probe station is compared to the theoretical expectation, which was calculated using the temperature measurement. The temperature was measured at each point of the IV curve. Furthermore, the mean value of the measured and the theoretically expected ratios as well as the maximum and the mean deviation of the measurements from the theory are recorded. For the calculation of these values, all measurement points except the first two have been taken into account, as the current ratio at low voltages shows large deviations from the theory, which is not representative for the rest of the measurement.

9.1.1. Results: Climate Chamber

Foundry 3

The IV curves of two irradiated sensors from Foundry 3 were measured in the climate chamber (CC). Sensor 1 was irradiated with 2×10^{15} n_{eq}/cm², sensor 2 with 5×10^{15} n_{eq}/cm². The current ratios for different temperature differences and the theoretical expectations are shown in Figure 9.2. Furthermore, the mean value of the measured and the theoretically expected ratios as well as the maximum and the mean deviation of the measurements from the theory are recorded in Table 9.1.

The temperature of a measurement is not necessarily constant, but can change while the measurement is made. The stated temperatures are the temperatures that are set in the beginning of the measurement, but for the calculation of the theoretical ratio the actually measured temperature was used.

9.1. Testing the Relative Temperature Dependence

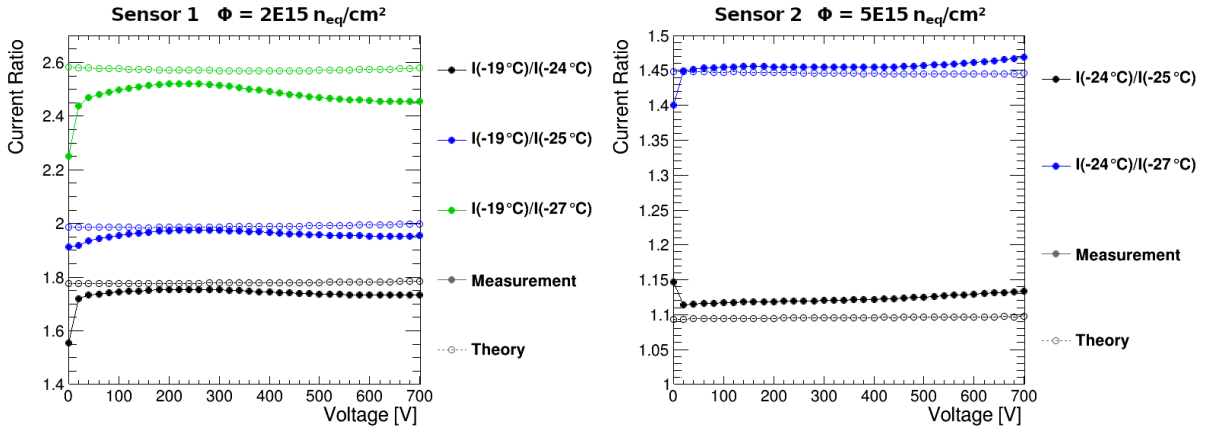


Figure 9.2.: Comparison of measured and theoretically expected current ratios of sensors from Foundry 3 (CC). Theoretical expectations are shown as open circles. Measurements are shown as closed circles.

Sensor $I(T_1)/I(T_2)$	Current Ratio		Mean Dev. [%]	Max. Dev. [%]
	Meas.	Theory		
Sensor 1				
$I(-19^\circ\text{C})/I(-24^\circ\text{C})$	1.74	1.78	1.9	2.8
$I(-19^\circ\text{C})/I(-25^\circ\text{C})$	1.96	1.99	1.3	2.5
$I(-19^\circ\text{C})/I(-27^\circ\text{C})$	2.49	2.57	3.2	4.7
Sensor 2				
$I(-24^\circ\text{C})/I(-25^\circ\text{C})$	1.21	1.10	2.3	2.8
$I(-24^\circ\text{C})/I(-27^\circ\text{C})$	1.46	1.45	0.6	1.1

Table 9.1.: Mean measured and theoretical current ratios and the mean and maximum deviation between them from measurements of sensors 1 and 2 (Foundry 3) at different temperatures (CC).

In both sensors, the measured current ratios are close to the theoretical expectation. The mean deviation does not exceed 3.2% and the maximum deviation is not higher than 4.7%. Both sensors are very similar in this context and there is no sign that the sensor with a higher irradiation level shows a bigger deviation of measurement from theory.

Foundry 4

The IV curves of four irradiated sensors from Foundry 4 were measured in the climate chamber. Sensor 1 and 2 were irradiated with $2 \times 10^{15} \text{ n}_{\text{eq}}/\text{cm}^2$ and sensor 3 and 4 with $5 \times 10^{15} \text{ n}_{\text{eq}}/\text{cm}^2$. Figure 9.3 shows the comparison of the measured and the theoretically expected current ratios for different temperature differences. The mean value of the

9. Relative Temperature Dependence of the Leakage Current in Irradiated Sensors

measured and the theoretically expected ratios as well as the maximum and the mean deviation of the measurements from the theory are recorded in Table 9.2.

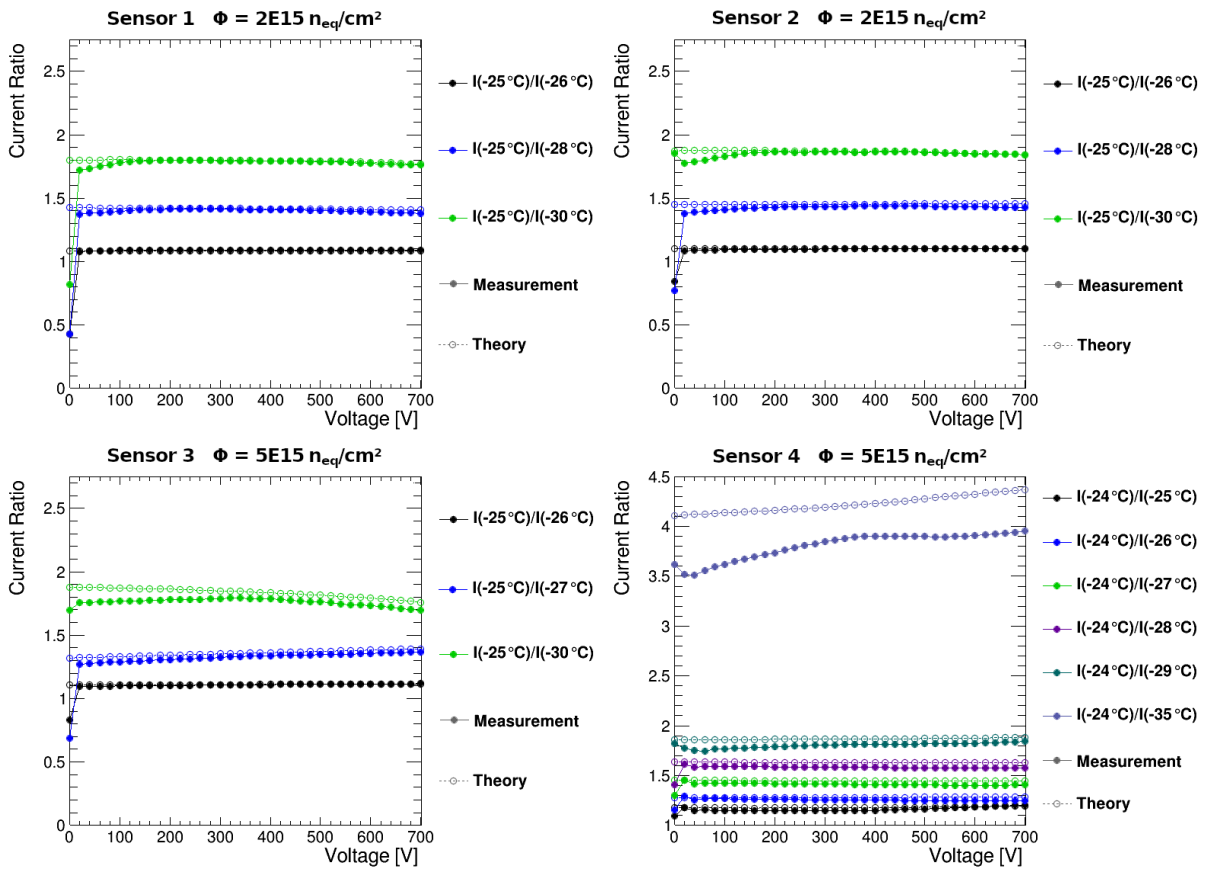


Figure 9.3.: Comparison of measured and theoretically expected current ratios of sensors from Foundry 4 (CC). Theoretical expectations are shown as open circles. Measurements are shown as closed circles.

9.1. Testing the Relative Temperature Dependence

Sensor $I(T_1)/I(T_2)$	Current Ratio		Mean Dev.[%]	Max. Dev.[%]
	Meas.	Theory		
Sensor 1				
$I(-25^\circ\text{C})/I(-26^\circ\text{C})$	1.09	1.08	0.5	0.6
$I(-25^\circ\text{C})/I(-28^\circ\text{C})$	1.40	1.42	0.9	3.0
$I(-25^\circ\text{C})/I(-30^\circ\text{C})$	1.79	1.80	0.6	3.7
Sensor 2				
$I(-25^\circ\text{C})/I(-26^\circ\text{C})$	1.10	1.10	0.3	1.2
$I(-25^\circ\text{C})/I(-28^\circ\text{C})$	1.43	1.45	1.8	4.4
$I(-25^\circ\text{C})/I(-30^\circ\text{C})$	1.85	1.87	0.9	5.0
Sensor 3				
$I(-25^\circ\text{C})/I(-26^\circ\text{C})$	1.11	1.11	0.4	1.3
$I(-25^\circ\text{C})/I(-27^\circ\text{C})$	1.32	1.35	2.4	3.7
$I(-25^\circ\text{C})/I(-30^\circ\text{C})$	1.77	1.84	4.1	6.6
Sensor 4				
$I(-24^\circ\text{C})/I(-25^\circ\text{C})$	1.16	1.18	2.0	2.6
$I(-24^\circ\text{C})/I(-26^\circ\text{C})$	1.26	1.28	1.9	2.9
$I(-24^\circ\text{C})/I(-27^\circ\text{C})$	1.41	1.45	2.5	3.2
$I(-24^\circ\text{C})/I(-28^\circ\text{C})$	1.58	1.63	3.0	3.6
$I(-24^\circ\text{C})/I(-29^\circ\text{C})$	1.80	1.87	3.8	6.6
$I(-24^\circ\text{C})/I(-35^\circ\text{C})$	3.80	4.21	10.8	17.3

Table 9.2.: Mean measured and theoretical current ratios and the mean and maximum deviation between them from measurements of sensors 1, 2, 3 and 4 (Foundry 4) at different temperatures (CC).

Overall, the measurements of sensors 1 and 2 (irradiated with $2 \times 10^{15} \text{ n}_{\text{eq}}/\text{cm}^2$) show a better match to the theory than both sensors from Foundry 3. The maximum deviations are in the same range (up to 5%), but the mean deviation is much smaller (less than 1% for most measurements). Sensors 3 and 4 (irradiated with $5 \times 10^{15} \text{ n}_{\text{eq}}/\text{cm}^2$) show larger deviations than the other sensors measured in the CC. Here, the mean deviation of the measurements from the theory increases with larger temperature differences (up to 10% in sensor 4). This hints at a larger share of edge and surface current in these sensors, probably caused by radiation damage on the surface.

9.1.2. Results: Probe Station

When measuring on the probe station (PS), the measured temperature is logged by a temperature sensor which is glued to the cooling chuck with Kapton tape and thermal grease. The sensor under test is also in direct contact with the temperature controlled chuck. As this is not a closed system, like the climate chamber, the thermal contact between temperature sensor and chuck needs to be very good to get accurate temperature measurements. However, this is only possible to a certain degree. For that reason the measured temperature often deviates from the temperature that was set on the cooling chuck. The set temperature, on the other hand, does not represent the exact measurement temperature, because the chiller is cooling the chuck and the sensor cyclically, which results in temperature fluctuations around the set temperature.

So there are two ways to calculate the theoretically expected current ratio: Taking the set temperature, which should be more accurate for the absolute temperature dependence or taking the temperature measurement, which is often higher than the actual temperature, but is sensitive to temperature fluctuations due to the cycle of the chiller. In the following, both options are used and compared to the measured current ratio for sensors from Foundry 3 and 4, which were measured on the probe station.

Foundry 3

In most of the measurements of sensors from Foundry 3 on the probe station, the thermal contact between the temperature sensor and the chuck was not optimal. Therefore, the measured temperature is approximately 7°C higher than the set temperature and the comparison of the measured and the theoretically expected current ratio cannot reveal any sensor specific behaviour.

An example of the comparison for sensor 1 ($\Phi = 2 \times 10^{15} \text{ n}_{\text{eq}}/\text{cm}^2$) is shown in Figure 9.4.

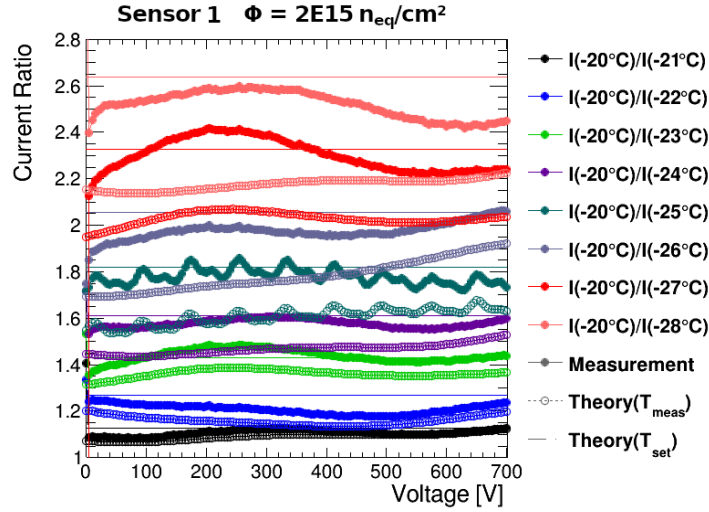


Figure 9.4.: Comparison of measured and theoretically expected current ratios of sensor 1 from Foundry 3 (PS). Theoretical expectations calculated from the measured temperature are shown as open circles and theoretical expectations calculated from the set temperature are shown as horizontal straight lines. Measurements are shown as closed circles.

Despite the deviation of the measured from the set temperature, the theoretically calculated current ratios from the measured temperatures still give good approximations for small temperature differences ($1 - 2^\circ\text{C}$). They roughly follow the shape of the measured current ratio except for an offset. This offset increases with growing temperature differences.

The theoretical current ratio calculated with the set temperature roughly matches the average absolute value of the current ratio of the measurements, but due to the temperature fluctuations caused by the cycle of the chiller, the deviations are still large at most points of the measurement. In most measurements only one period of the chiller cycle can be seen. In the measured ratio of $I(-20^\circ\text{C})/I(-25^\circ\text{C})$, on the other hand, several periods are visible as the measurement at -25°C was taken with a longer waiting time between the measurements. Here, the theoretical expectation calculated with the set temperature is closer to the mean value of the measured current ratio than in most other measurements.

Foundry 4

Four irradiated sensors from Foundry 4 were measured on the probe station. For sensor 1, no measurements at different temperatures after the same time of annealing were made, so this sensor is left out of the comparison.

Sensor 2 was irradiated with $2 \times 10^{15} \text{ n}_{\text{eq}}/\text{cm}^2$ and sensors 3 and 4 with $5 \times 10^{15} \text{ n}_{\text{eq}}/\text{cm}^2$. In Figure 9.5, the measured and the theoretically expected current ratios (calculated from

9. Relative Temperature Dependence of the Leakage Current in Irradiated Sensors

the set and the measured temperature) are shown for different temperature differences. In Table 9.3, the mean values for the measured and the two theoretically calculated current ratios as well as the mean and maximum deviation of the measured ratios from both of the theoretical ratios are shown for sensors 2, 3 and 4.

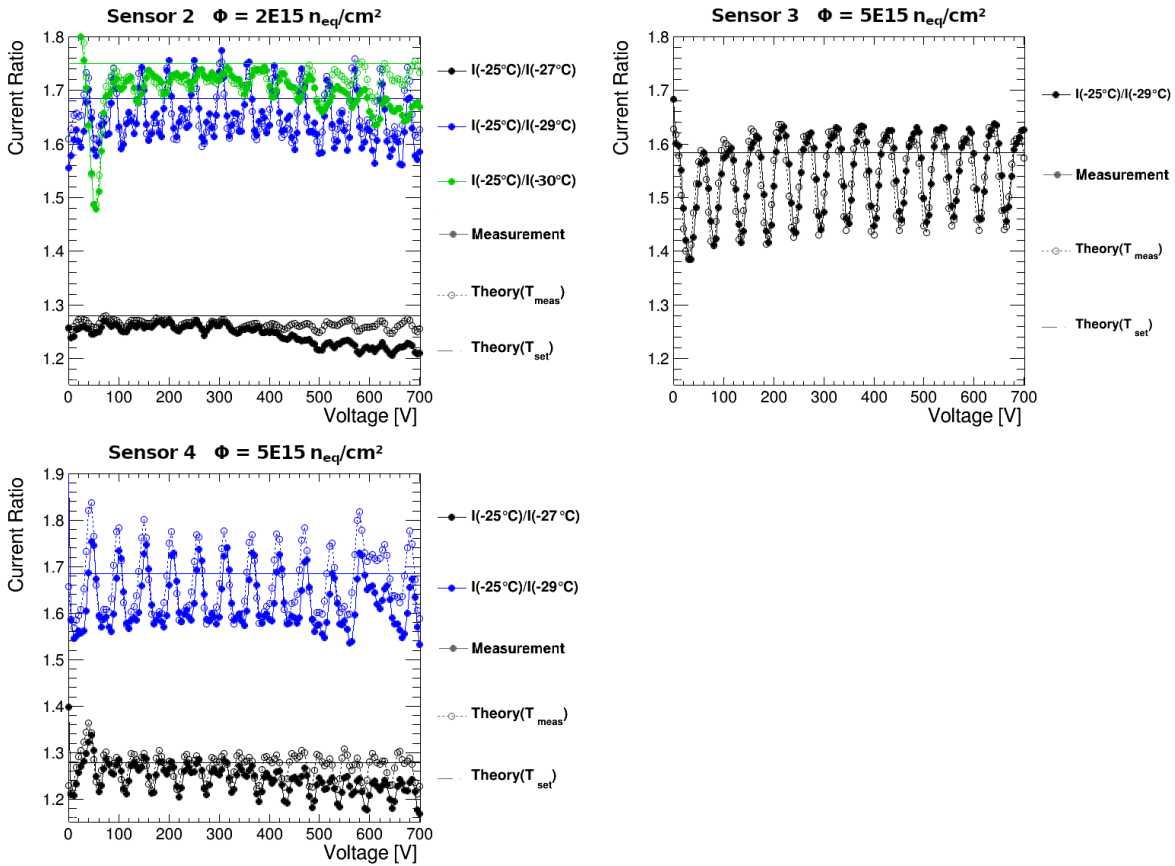


Figure 9.5.: Comparison of measured and theoretically expected current ratios of sensors from Foundry 4 (PS). Theoretical expectations calculated from the measured temperature are shown as open circles and theoretical expectations calculated from the set temperature are shown as straight lines. Measurements are shown as closed circles.

Sensor $I(T_1)/I(T_2)$	Current Ratio		Mean Dev.[%]		Max. Dev.[%]		
	Measured (T_{meas})	Theory (T_{set})	of theoretical from measured ratio (T_{meas}) (T_{set})		(T_{meas})	(T_{set})	
Sensor 2							
$I(-25^\circ\text{C})/I(-27^\circ\text{C})$	1.25	1.26	1.28	1.5	2.7	3.9	6.1
$I(-25^\circ\text{C})/I(-29^\circ\text{C})$	1.65	1.66	1.68	1.4	3.3	4.8	7.9
$I(-25^\circ\text{C})/I(-30^\circ\text{C})$	1.70	1.71	1.75	1.1	3.3	4.7	18.3
Sensor 3							
$I(-25^\circ\text{C})/I(-27^\circ\text{C})$	1.24	1.27	1.28	2.6	3.2	6.1	8.7
$I(-25^\circ\text{C})/I(-29^\circ\text{C})$	1.62	1.66	1.68	2.9	4.7	8.8	9.6
Sensor 4							
$I(-25^\circ\text{C})/I(-29^\circ\text{C})$	1.54	1.54	1.58	1.9	4.2	4.5	14.4

Table 9.3.: Mean measured and theoretical (calculated with measured and set temperature) current ratios and the mean and maximum deviation between them from measurements of sensors 2, 3 and 4 (Foundry 4) at different temperatures (PS).

The measured current ratios match the theoretical ratio calculated with the measured temperature very well for all temperature differences (mean deviation of 1 – 3%). The mean and maximum deviation are even smaller than the mean and maximum deviation from the theoretical value calculated with the set temperature. The reason for this is that the thermal contact of the temperature sensor to the cold chuck was better when the measurements of the sensors from Foundry 4 were made. The measured temperature is only about 1°C higher than the set temperature. Given better thermal contact, using the measured temperature which reflects temperature fluctuation during the measurement, gives a better theoretical expectation than using the temperature that was set in the beginning.

9.1.3. Comparison of the Results from the Climate Chamber and the Probe Station

When comparing the results from the measurements in the climate chamber to the results from the measurements on the probe station for the sensors from Foundry 4, it is visible that for both methods the deviations of the measured current ratio from the theoretical current ratios calculated with the measured temperature are of the same size. This means that the thermal contact in the probe station measurements of sensors from Foundry 4

9. Relative Temperature Dependence of the Leakage Current in Irradiated Sensors

was good enough to give an accurate temperature measurement.

In the probe station measurements of sensors from Foundry 3, this was not the case, however, the theoretically calculated current ratios can still qualitatively explain the behaviour of the measured current ratios.

9.2. Scaling IV Curves to a Reference Temperature

Based on Equation 9.1, a current at a certain measurement temperature T can be scaled to another temperature T_{ref} by using

$$I(T_{\text{ref}}) = I(T) \cdot \exp\left(\frac{E_g(T_{\text{ref}} - T)}{2kT_{\text{ref}}}\right). \quad (9.2)$$

Scaling each point of an IV curve to T_{ref} should yield a curve similar to a measurement which was actually made at T_{ref} .

As for this method the exact temperature of the measurement is needed, it is best to test this on IV curves which were measured in the climate chamber. Figure 9.6 shows IV curves of two irradiated sensors from Foundry 4 (sensors 2 and 4), which were measured at different temperatures and then scaled to a reference temperature. Sensor 2 was irradiated with $2 \times 10^{15} \text{ n}_{\text{eq}}/\text{cm}^2$ and sensor 4 with $5 \times 10^{15} \text{ n}_{\text{eq}}/\text{cm}^2$.

It can be shown that the scaled and reference IV curve match closely for both sensors. The match is closer for sensor 2 which was irradiated with a lower fluence.

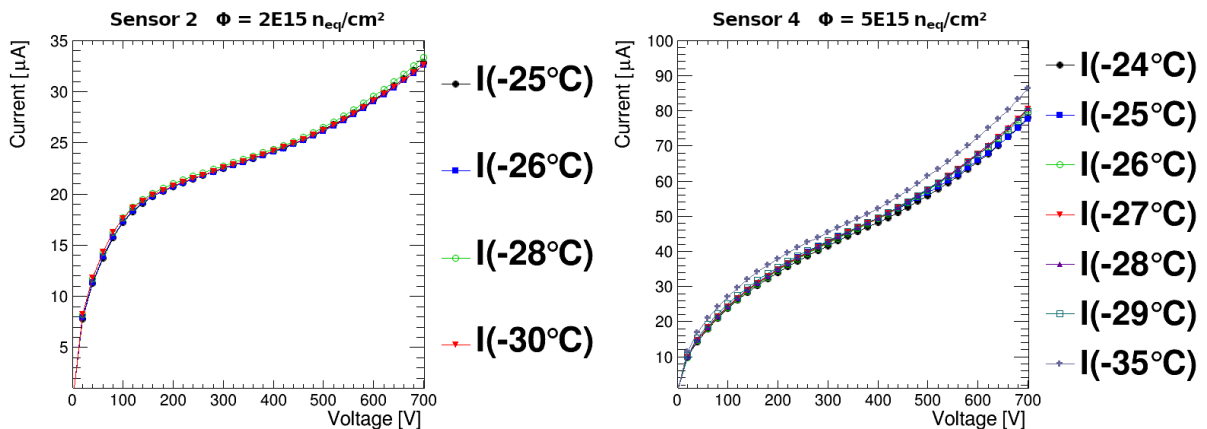


Figure 9.6.: IV curves of sensor 2 and 4 (Foundry 4) scaled to -25°C and a reference IV curve measured at -25°C (CC). The temperature in parentheses is the set temperature of the measurements.

For sensors measured on the probe station it was hoped to use this scaling method to

9.2. Scaling IV Curves to a Reference Temperature

correct for the fluctuations in the leakage current caused by the fluctuating temperature due to the cycle of the chiller. For this purpose the points of the IV curves are scaled to the mean temperature of the measurement. This was tested on two irradiated sensors from Foundry 4, as the thermal contact was best in these measurements, which gives a more precise temperature readout than in the measurements of sensors from Foundry 3. The result is shown in Figure 9.7.

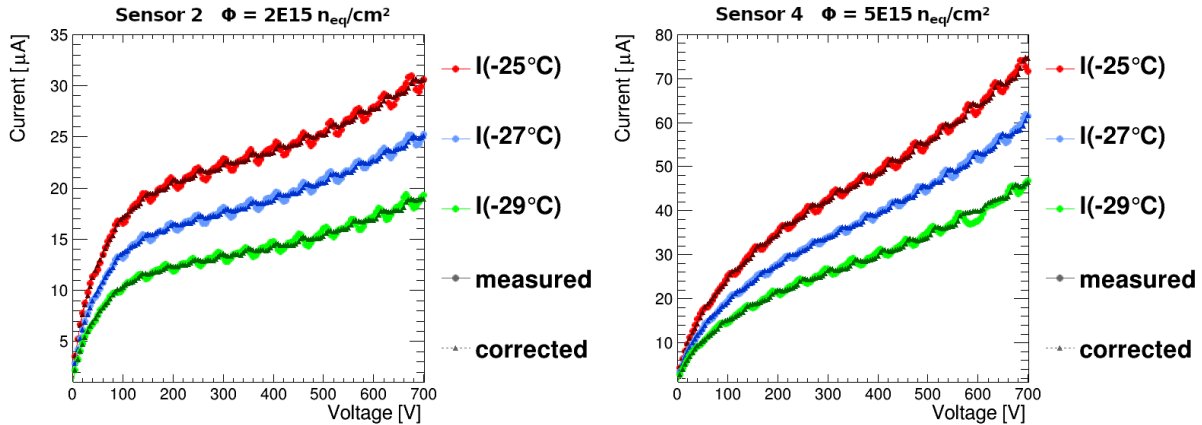


Figure 9.7.: Raw measured IV curves and IV curves scaled to the mean temperature of the measurement of sensors from Foundry 4 (PS).

The temperature in parentheses is the set temperature of the measurement.

It is visible that the corrected curves are smoother than the original ones, but small fluctuations remain. It also seems as if the peaks and valleys of the scaled curves are shifted forward by a few volts. So, although the temperature dependence of these measurements match the theoretical expectation closely (see Section 9.1.2), the thermal contact of the temperature sensor is still not good enough or the share of edge and surface current is too high to use this method to fully correct IV curves measured on the probe station for the chiller cycle fluctuations.

10. Summary

In this thesis, the capacitance-voltage-characteristics and the current-voltage-characteristics of planar Silicon pixel sensors, which were developed for the ATLAS ITk upgrade, were studied. The analysed measurements were made in Göttingen in the course of the ongoing market survey to find suitable foundries for production.

An algorithm to determine the depletion voltage from CV curves and an algorithm to detect a breakdown and determine the breakdown voltage from IV curves have been developed. Furthermore, the dependencies of the leakage current in irradiated sensors on the measurement temperature, the fluence and the annealing time have been studied and compared to the theoretical expectations.

For the algorithm to automatically determine the depletion voltage from measured CV curves, two methods were developed. The methods differ by the functions that were fitted to the CV curve. In method 1 two straight lines are fitted and in method 2 a continuous function consisting of a sloped and a constant section is fitted to the measurements. The fit parameters of both methods are initialised with a pre-fit of two straight lines to small sections of the curve. Both methods converge and give similar results for the measurements that were tested. As CV curves always have a similar appearance (slope in the front, constant in the back), there is no need to change the range of the fit from the default values. The only parameter that might need to be set manually is the width of the curved section of the CV curve if method 1 is used. For the measurements that were tested, the default value and some variations of this value give consistent results, however, more testing on sensors with different CV behaviour (e.g. wider curved section) would be needed to find out if this is always the case.

For the algorithm to automatically find the breakdown voltage from an IV curve, five options were implemented. The options 1-3, which were derived from definitions of V_{BD} from ITk documents, work well for hard breakdowns above the depletion voltage, but are not reliable for a different breakdown behaviour. Sometimes a small increase of current in an otherwise smooth IV curve triggers a criterion and is detected as a breakdown and

10. Summary

sometimes an obvious breakdown triggers none or only some of the criteria. Definition 2 (search for the exceedance of a defined slope) seems to be the most reliable option, but it cannot detect breakdown voltages lower than the depletion voltage. Therefore, option 4 (search for the crossing of a defined current threshold) and option 5 (search for the exceedance of a defined slope backwards from the voltage that option 4 returns) were added and it was found that the combination of option 2 and 4 can reliably detect a breakdown and find the breakdown voltage. With different values for the slope and the current threshold, this combination can probably also be used to find the breakdown voltage in irradiated sensors, however this has not been tested.

When analysing the absolute leakage current in sensors after irradiation, it was shown that the current related radiation damage roughly matches the theoretical expectation of a linear fluence dependence. Two irradiated sensors show a breakdown. Furthermore, the IV curves that were measured after different annealing periods roughly follow the expected dependence [5].

The comparison of the measured to the theoretical temperature dependence of the leakage current in irradiated sensors shows a good match within typically a few percent for measurements in the climate chamber and on the probe station - if the thermal contact between temperature sensor and chuck was good. The temperature that was measured during the current measurement can be used to scale IV curves to different temperatures. However, it is not accurate enough or the temperature dependence does not match the theory close enough to use this method to correct the probe station measurements for the temperature fluctuations that are caused by the chiller cycle.

A. Algorithm to Determine the Depletion Voltage

```
//determine Vdep from 1/C2 curve (method 1)
//(define fitting range and curveWidth as voltages)
void getVdepFrom1overC2VoltDefine(TGraphErrors* gr,
double slopeBegin, double slopeEnd, double constBegin,
double constEnd, double curveWidth, double Vdep[]){

    //define fitting functions
    TF1 *slope = new TF1 ("slope", "[0]*x+[1]", 0,250);
    slope->SetParameters(1,1);
    TF1 *constant = new TF1 ("constant", "[0]",0,250);
    constant->SetParameter(0, 1);
    //prefit
    gr->Fit("slope","QW","",slopeBegin, slopeEnd);
    gr->Fit("constant","QW+","",constBegin, constEnd);

    //calculate Vdep, approx from intersection of
    //...the prefit functions
    double m = slope->GetParameter(0);
    double b = slope->GetParameter(1);
    double c = constant->GetParameter(0);
    Vdep[0] = (c-b)/m;

    //final fit
    //(using option M to improve fit with TMinuit algorithm)
    gr->Fit("slope","Q","", slopeBegin, Vdep[0]-curveWidth/2);
    gr->Fit("constant","Q+","",Vdep[0]+curveWidth/2, constEnd);
    gr->Fit("slope","QM","", slopeBegin, Vdep[0]-curveWidth/2);
    gr->Fit("constant","QM+","",Vdep[0]+curveWidth/2, constEnd);
}
```

A. Algorithm to Determine the Depletion Voltage

```
//calculate Vdep from final fit
m = slope->GetParameter(0);
b = slope->GetParameter(1);
c = constant->GetParameter(0);
Vdep[0] = (c-b)/m;

//calculate statistical fitting error of Vdep
double mErr = slope->GetParError(0);
double bErr = slope->GetParError(1);
double cErr = constant->GetParError(0);
Vdep[1]=sqrt(pow(mErr*2*(c-b)/(m*m),2)+pow(bErr/m, 2)
+pow(cErr/m, 2));

//draw fitted functions
TF1 *slopeDraw = new TF1("slopeDraw", "[0]*x+[1]",0,200);
slopeDraw->SetParameters(m, b);
TF1 *constantDraw = new TF1("constantDraw", "[0]",0,200);
constantDraw->SetParameter(0, c);
slopeDraw->Draw("same");
constantDraw->Draw("same");

return;
}

//determine Vdep from 1/C2 curve (method 1)
//(define fitting range and curveWidth as # of points,
//...calls ..VoltDefine)
void getVdepFrom1overC2PointDefine(TGraphErrors* gr,
int cutStart, int cutEnd, int useStart, int useEnd,
int curvedPoints, double Vdep[]){
//cutStart = cut #points from beginning of gr
//cutEnd = cut #points from end of gr
//useStart = use #points from beginning of cut gr to fit slope
//useEnd = use #points from end of cut gr to fit constant
//curvedPoints = #points in curved area, cut from final fit
double slopeBegin = gr->GetX(cutStart+1);
double slopeEnd = gr->GetX(cutStart+useStart+1);
double constBegin = gr->GetX(gr->GetN()-cutEnd-useEnd);
double constEnd = gr->GetX(gr->GetN()-cutEnd-1);
double curveWidth = (gr->GetX(cutStart+1)
```

```

-gr->GetPointX(cutStart))*curvedPoints;
getVdepFrom1overC2VoltDefine(gr, slopeBegin, slopeEnd,
constBegin, constEnd, curveWidth, Vdep);
return;
}

//determine Vdep from 1/C2 curve (method 1)
//(default values for fitting range and curveWidth as # of points,
//...calls ..PointDefine)
void getVdepFrom1overC2(TGraphErrors* gr, double Vdep[]){
int cutStart = 2;
int cutEnd = 2;
int useStart = 6;
int useEnd = 6;
int curvedPoints = 2;
getVdepFrom1overC2PointDefine(gr, cutStart, cutEnd, useStart,
useEnd, curvedPoints, Vdep);
return;
}

//function for getVdepFrom1overC2 method 2
Double_t myfunc (Double_t *x, Double_t *par){
Double_t xx=x[0];
if(xx<par[0]) return par[1]*xx+par[2]-par[0]*par[1];
else return par[2];
}

//determine Vdep from 1/C2 curve (method 2)
//(define fitting range as voltages)
void getVdepFrom1overC2VoltDefineMyfunc(TGraphErrors* gr,
double slopeBegin, double slopeEnd, double constBegin,
double constEnd, double Vdep[]){

//define functions for prefit
TF1 *slope = new TF1 ("slope", "[0]*x+[1]", 0,250);
slope->SetParameters(1,1);
TF1 *constant = new TF1 ("constant", "[0]",0,250);
constant->SetParameter(0, 1);

```

A. Algorithm to Determine the Depletion Voltage

```
//prefit
gr->Fit("slope","QW","",slopeBegin, slopeEnd);
gr->Fit("constant","QW+","",constBegin, constEnd);

//read out fit parameters of prefit and calculate Vdep, approx
double m = slope->GetParameter(0);
double b = slope->GetParameter(1);
double c = constant->GetParameter(0);
Vdep[0] = (c-b)/m;

//initiate function for final fit
TF1 *func = new TF1 ("func", myfunc, 0,250,3);
func->SetParameters(Vdep[0], m, c);

//final fit
gr->Fit("func","", "", slopeBegin, constEnd);
TF1 *funcResult = (TF1*) gr->GetFunction("func");

//readout Vdep and stat. fit error
Vdep[0] = func->GetParameter(0);
Vdep[1] = func->GetParError(0);

return;
}

//determine Vdep from 1/C2 curve (method 2)
//(define fitting range as # of points,
//...calls ..MyfuncVoltDefine)
void getVdepFrom1overC2PointDefineMyfunc(TGraphErrors* gr,
int cutStart, int cutEnd, int useStart, int useEnd, double Vdep[]){
//cutStart = cut #points from beginning of gr
//cutEnd = cut #points from end of gr
//useStart = use #points from beginning of cut gr to fit slope
//useEnd = use #points from end of cut gr to fit constant
double slopeBegin = gr->GetPointX(cutStart+1);
double slopeEnd = gr->GetPointX(cutStart+useStart+1);
double constBegin = gr->GetPointX(gr->GetN()-cutEnd-useEnd);
double constEnd = gr->GetPointX(gr->GetN()-cutEnd-1);
getVdepFrom1overC2VoltDefineMyfunc(gr, slopeBegin, slopeEnd,
```

```

    constBegin, constEnd, Vdep);
    return;
}

//determine Vdep from 1/C2 curve (method 2)
// (default values for fitting range as # of points,
// ... calls ..MyfuncPointDefine)
void getVdepFrom1overC2Myfunc(TGraphErrors* gr, double Vdep[]){
    int cutStart = 2;
    int cutEnd = 2;
    int useStart = 6;
    int useEnd = 6;
    getVdepFrom1overC2PointDefineMyfunc(gr, cutStart, cutEnd, useStart,
    useEnd, Vdep);
    return;
}

```


B. Algorithm to Determine the Breakdown Voltage

```
//find breakdown voltage (only works for 5V-step-measurements)
double findVBD(TGraph *gr, string opt, double slopeDef,
double threshold, double Vdep){
    double *I = gr->GetY();
    double *V = gr->GetX();
    double Istep = 0;
    double Vstep = 0;

    for(int i=0; i<gr->GetN(); i++){
        //search for increase of 20% above Vdep
        if(i+1<gr->GetN() && opt=="option1"){
            if ((I[i+1]/I[i])>1.2 && V[i]>Vdep){
                return V[i];
            }
        }
        //search for grow rate > slopeDef above Vdep
        if(i+1<gr->GetN() && opt=="option2"){
            Vstep = V[i+1]-V[i];
            Istep = I[i+1]-I[i];
            if(Istep/Vstep>slopeDef && V[i]>Vdep){
                return V[i];
            }
        }
        //search for increase of 100% above Vdep
        if(i+2<gr->GetN() && opt=="option3"){
            if(I[i+2]/I[i+1]>2 && V[i]>Vdep){
                return V[i];
            }
        }
    }
}
```

B. Algorithm to Determine the Breakdown Voltage

```
//searches for crossing of threshold
if(opt=="option4"){
    if(I[i]>threshold){
        return V[i];
    }
}
//searches for crossing of threshold
if(opt=="option5"){
    if(I[i]>threshold){
//...and from there backwards for grow rate < slopeDef
        for(int j=i; j>0; j--){
            Istep = I[j]-I[j-1];
            Vstep = V[j]-V[j-1];
            if(Istep/Vstep < slopeDef) return V[j];
        }
        return 0;
    }
}
}
return -1111; //VBD=-1111 means that the chosen option
} //...does not detect a breakdown
```

Bibliography

- [1] ATLAS Collaboration, *Observation of a new particle in the search for the Standard Model Higgs boson with the ATLAS detector at the LHC*, Phys. Lett. B **716**, 1 (2012)
- [2] CMS Collaboration, *Observation of a New Boson at a Mass of 125 GeV with the CMS Experiment at the LHC*, Phys. Lett. B **716**, 30 (2012)
- [3] L. Evans, P. Bryant, *LHC Machine*, JINST **3**, S08001 (2008)
- [4] ATLAS Collaboration, *The ATLAS Experiment at the CERN Large Hadron Collider*, JINST **3**, S08003 (2008)
- [5] M. Moll, *Radiation damage in silicon particle detectors: Microscopic defects and macroscopic properties*, Ph.D. thesis, Hamburg University (1999)
- [6] ATLAS Collaboration, *Technical Design Report for the ATLAS Inner Tracker Pixel Detector*, Technical Report CERN-LHCC-2017-021. ATLAS-TDR-030, CERN, Geneva (2017)
- [7] A. Dimitrievska, A. Stiller (RD53), *RD53A: A large-scale prototype chip for the phase II upgrade in the serially powered HL-LHC pixel detectors*, Nucl. Instrum. Meth. **A958**, 162091 (2020)

Danksagung

Ohne die Unterstützung einiger Menschen wäre diese Arbeit wohl niemals entstanden. Dafür möchte ich Danke sagen.

Zunächst natürlich an Prof. Dr. Arnulf Quadt, dafür, dass er mir die Chance gegeben hat, meine Bachelorarbeit in seiner Arbeitsgruppe zu schreiben und trotz der derzeitigen Situation einen kleinen Einblick in das wissenschaftliche Arbeiten zu erhalten - wenn auch nur über Vidyó. In dem Zuge möchte ich auch Priv.Do. Dr. Jörn Große-Knetter dafür danken, dass das Arbeiten von Zuhause durch den Zugriff auf die Labor PCs überhaupt so reibungslos funktioniert hat und auch kleinere Probleme schnell gelöst waren.

Mein größter Dank geht an Silke Möbius und Dr. Jörn Lange, die mir immer mit Rat und Tat und vor allem viel Geduld zur Seite gestanden haben. Ohne euch wäre diese Arbeit nicht halb so gut geworden, und das nicht nur, weil ich ohne euch keine Messungen zum Untersuchen gehabt hätte.

Natürlich möchte ich auch von ganzem Herzen meinen Eltern und meinem Bruder dafür danken, dass sie mich nun schon fast ein Vierteljahrhundert immer und auf jegliche Weise unterstützt haben. Danke für alles.

Zuletzt sage ich noch Danke an meine Freunde, einfach dafür, dass ich mich auf euch verlassen kann.

Erklärung

nach §13(9) der Prüfungsordnung für den Bachelor-Studiengang Physik und den Master-Studiengang Physik an der Universität Göttingen:

Hiermit erkläre ich, dass ich diese Abschlussarbeit selbständig verfasst habe, keine anderen als die angegebenen Quellen und Hilfsmittel benutzt habe und alle Stellen, die wörtlich oder sinngemäß aus veröffentlichten Schriften entnommen wurden, als solche kenntlich gemacht habe.

Darüberhinaus erkläre ich, dass diese Abschlussarbeit nicht, auch nicht auszugsweise, im Rahmen einer nichtbestanden Prüfung an dieser oder einer anderen Hochschule eingereicht wurde.

Göttingen, den 1. August 2020



(Johannes Weller)